J. Fluid Mech. (2000), *vol.* 405, *pp.* 1–36. Printed in the United Kingdom

Numerical investigation of reacting droplets in homogeneous shear turbulence

By FARZAD MASHAYEK

Department of Mechanical Engineering, University of Hawaii at Manoa, 2540 Dole Street, Honolulu, HI 96822, USA

(Received 7 May 1998 and in revised form 10 September 1999)

Numerical simulations are performed of a compressible oxidizer gas laden with fuel droplets. The carrier phase is considered in the Eulerian context and is simulated via direct numerical simulation (DNS). The fuel droplets are tracked in the Lagrangian frame and interactions between the two phases are taken into account in a realistic two-way coupled formulation. It is assumed that combustion takes place in the vapour phase, resulting in a 'homogeneous' reaction described by *fuel* + *oxidizer* → *products* + *energy*. Several simulations are performed within the configuration of low-Mach-number homogeneous shear turbulence to investigate the effects of the mass loading ratio, the droplet time constant, the Damköhler number, and the heat release coefficient. Initial mass loading ratios up to 0.8 and initial Stokes numbers (based on the Kolmogorov time scale) of 1.23 and 2.46 are considered. The results of these simulations along with those from non-reacting cases are utilized to analyse the droplet size distribution, the fuel vapour, the oxidizer, and the reaction rate and zone. An analysis of the statistics of the two-phase flow indicates that various fields are accurately resolved and the assumptions invoked in the formulation of the problem are satisfied. The mean evaporation rate (normalized with the initial mass of the droplets) decreases with the increase of either the mass loading ratio or the droplet time constant. It is shown that the droplet size distribution can be reasonably approximated by a Gaussian probability density function (p.d.f.) for all of the cases. The joint p.d.f. of the fuel vapour and the oxidizer mass fractions exhibits the features of a premixed reaction. The values of the Taylor microscale of the fuel vapour and the oxidizer are closer in the presence of the chemical reaction than in the evaporating but non-reacting case. The reaction rate exhibits higher values in the regions of the flow containing the droplets while experiencing moderate increase in the high-strain-rate regions. The evaporation rate (per mass of the droplet) is smaller for larger droplets but an opposite trend is observed for the reaction rate. The reaction zone tends to align with the streamwise direction due to the effects of the mean flow on the droplets. The alignment is enhanced with either the increase of the mass loading ratio or the decrease of the droplet time constant, or the decrease of the Damköhler number. The alignment of the fuel vapour and the oxidizer with the mean flow direction decreases and increases, respectively, as a result of the chemical reaction.

1. Introduction

This paper presents some recent results from a systematic investigation undertaken for modelling and numerical simulation of two-phase turbulent flows. The overall objective of the investigation is to provide a better physical understanding and a

more accurate treatment of the phenomenon of spray combustion which involves the atomization of the fuel into droplets followed by their evaporation and chemical reaction of the fuel vapour with the oxidizer. Due to the complexity of the problem, however, it was necessary to adopt a systematic approach and to study each of the above stages separately. Our previous studies (see Mashayek (1998*a*), and references therein) along with those by others (discussed in recent reviews by McLaughlin 1994; Eaton & Fessler 1994; Crowe, Troutt & Chung 1996) have been very helpful in understanding the mechanism of dispersion and polydispersity in particle-laden flows, without the added complexity of the chemical reaction.

The focus of this study is on numerical simulation of evaporating and reacting droplets dispersed in a compressible carrier phase. The carrier phase is treated in the Eulerian frame via direct numerical simulation (DNS) whereas the droplets are tracked in a Lagrangian manner. Since this is the first attempt in implementing DNS for the study of the reacting droplets dispersed in turbulent flows with two-way coupling, the problem is formulated based on models and correlations which are relatively well-established. It must be also emphasized that the term 'DNS' is used here with the understanding that there are models involved in describing the coupling between the two phases. Due to the presence of the droplets the flow is 'heterogeneous'; however, the combustion is assumed to take place in the vapour phase, thus rendering a 'homogeneous' reaction. For the range of the mass loading ratios used here, this assumption is reasonable (Chiu & Liu 1977). The flow considered is a homogeneous shear turbulence at low Mach numbers to avoid the extra complexity in dealing with shocklets.

Previous DNS of single-phase compressible flow has been carried out via both high-order finite difference (Lee, Lele & Moin 1991) and spectral (Passot & Pouquet 1987; Kida & Orszag 1990, 1992; Blaisdell, Mansour & Reynolds 1993; Miura & Kida 1995; Sarkar, Erlebacher & Hussaini 1991, 1992; Sarkar 1994) schemes. The numerical methodologies used in these studies are on firm grounds and can be extended to two-phase flows. The application of DNS to single-phase reacting flows was pioneered by Hill (1979) and has been collected in several reviews (e.g. Givi 1989, 1994). The data generated by DNS have been used for assessing various models (Givi & McMurtry 1988; McMurtry & Givi 1989; Gao & O'Brien 1991) and for analysing the structure of the reaction zone (Nomura & Elgobashi 1992; Leonard & Hill 1992; Swaminathan, Mahalingam & Kerr 1993, 1996). Both incompressible (Jaberi *et al.* 1997) and compressible (McMurtry *et al.* 1986; Menon & Fernando 1990; Balakrishnan, Sarkar & Williams 1995) flows have been considered.

The extent of the previous DNS studies of two-phase flows is too broad to be discussed here in detail. These previous studies are categorized based on flow configuration and coupling between the phases in table 1. As expected, the isotropic flows have been the subject of a large number of studies, due to their simple configuration. The inhomogeneous channel flows have also received a great deal of attention in the light of their extensive technological applications. The study of the two-way coupling in these flows, however, has been only recently initiated by Pan & Banerjee (1996). The homogeneous, anisotropic flows, due to their unsteady and anisotropic nature, provide a convenient configuration to be used for modelling of two-phase turbulent flows with both one- and two-way couplings. However, as table 1 indicates, the number of studies devoted to these flows is somewhat limited as compared to the other flow configurations. The majority of the studies shown in table 1 consider the dispersion of solid particles only. It has been very recently that we (Mashayek *et al.* 1997) studied dispersion and polydispersity of evaporating droplets

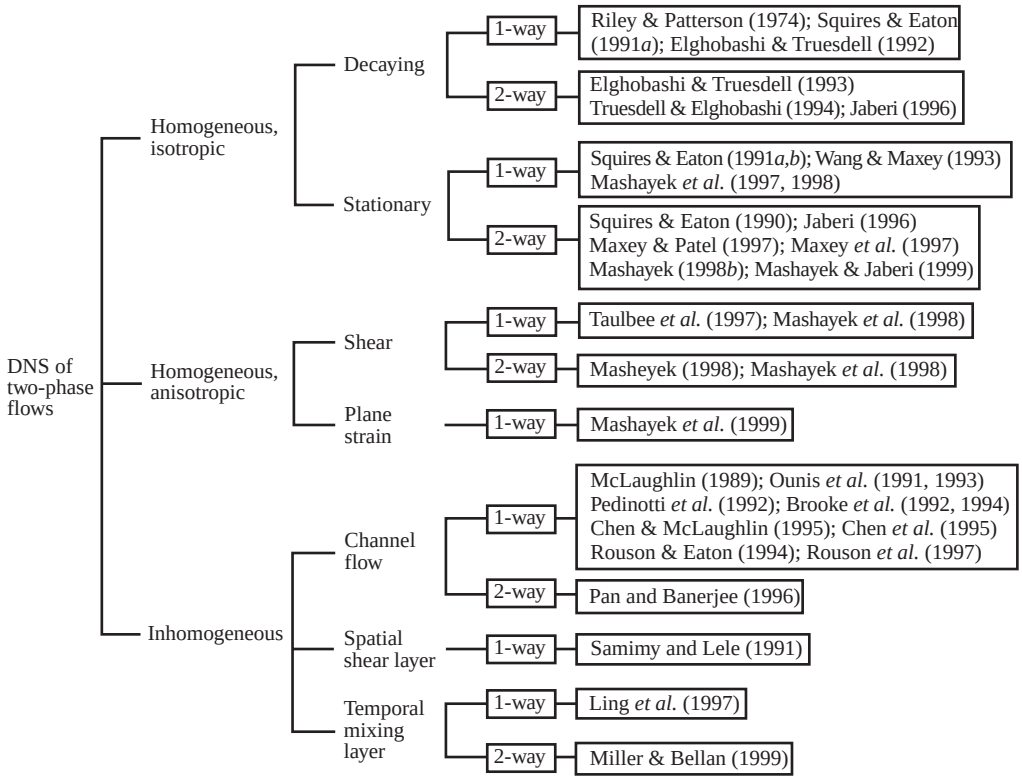

TABLE 1. Previous works on the DNS of two-phase flows.

in one-way coupling with an incompressible carrier phase. Later, Mashayek (1998*a*, *b*) relaxed some of the major assumptions invoked in the study of Mashayek *et al.* (1997) by considering two-way coupling and compressible flows.

A major issue in the simulation of two-phase flows including consideration of two-way coupling is the treatment of the effects of the dispersed phase on the carrier phase as the former is considered in the Lagrangian frame and the latter is described in the Eulerian context. In most of the applications, these effects are considered as point sources concentrated at the centre of the particle. In the particle-source-in-cell (PSI-Cell) method (Crowe, Sharma & Stock 1977) an Eulerian representation for these Lagrangian point sources is obtained by adding the effects of all of the particles residing inside a cell volume centred around each node. When implemented in conjunction with spectral methods, this procedure is successful provided that the number of particles is large and the spatial variation of the source term is small. Otherwise, large changes in the magnitude of the source term from one node to another may cause resolution problems. Recently, Maxey *et al.* (1997) adopted a somewhat different approach which provides a more smooth distribution of the source term within the simulation domain. This approach is also based on the point source concept; however, in transforming from the Lagrangian frame to the Eulerian the source term is distributed over an envelope centred at the particle position. The envelope gives a local spatial average or filtering which can be controlled by adjusting

the magnitude of a parameter. In the study of two-way coupling effects in a two-phase channel flow where the density ratio is about 1, Pan & Banerjee (1996) argue that in order to correctly account for the near-wall boundary conditions the particle-generated velocity disturbance in the carrier phase should be directly considered. However, it is mentioned that for unbounded flows with large density ratio the local disturbance velocity field due to particles is not important and the PSI-Cell model is successful. In the present work, we are dealing with homogeneous flows and large density ratios in which the diameter of the droplets is much smaller than the cell size. The PSI-Cell model is used for the calculation of the droplet source terms and it is shown, via analysis of various spectra, that for the parameter values considered in this study the pseudospectral method is able to accurately resolve all the Eulerian fields.

This work extends the study of Mashayek (1998*a*) on evaporating droplets in homogeneous shear turbulence by including the chemical reaction between the fuel vapour and an oxidizer carrier phase. The number of parameters involved in the formulation of the problem is too large to allow a detail parametric study. Here, we investigate the effects of the mass loading ratio, the droplet time constant, the Damköhler number, and the heat release coefficient. The results of Mashayek (1998*a*) and several preliminary simulations (not included here) have been used for choosing the appropriate values for the parameters involved. While various aspects of the two-phase flow can be investigated using the results of the simulations, since this is the first DNS study on reacting droplets the main attention is focused on the evolution of the reactants and the structure of the reaction zone. In the next section, the formulation of the problem and the numerical methodology are described. An overview of the simulations is provided in § 3 followed by the discussion of the droplet size and scalar fields in § 4, and the reaction rate and zone in § 5. A summary and some concluding remarks are furnished in § 6.

2. Formulation and methodology

This work deals with numerical simulation of homogeneous turbulent shear flow of a compressible (oxidizer) gas laden with (fuel) droplets. For the dilute two-phase flow considered here, it can be assumed that the chemical reaction is in the continuous phase where the fuel vapour and the oxidizer are mixed (Chiu & Liu 1977). Since this is the first numerical study of reacting droplets via implementation of DNS for the continuous phase, we consider the single-step, second-order, irreversible reaction:

$$F + rO \xrightarrow{K_{fwd}} (1 + r)P, \tag{1}$$

where, F, O, and P represent the fuel vapour, the oxidizer, and the product, respectively, K_{fwd} is the forward reaction rate constant, and r is the stoichiometric coefficient.

The governing equations considered here are the compressible forms of the continuity, momentum, and energy equations for the continuous phase coupled with the Lagrangian equations for discrete droplets. Also, conservation equations (in the Eulerian frame) are considered for the mass fractions of the fuel vapour and the oxidizer. For simplicity, the fuel vapour and the product are assumed to have the same molecular weight, viscosity, mass diffusivity, and specific heat as those of the oxidizer gas. In this manner, the mixture of the gas, the fuel vapour, and the product (hereinafter also referred to as the 'carrier phase' or the 'fluid') is treated as one entity – the continuity, momentum, and energy equations are solved for the mix-

ture. The specific enthalpies of the vapour and the product, however, are considered to be different than that of the gas in order to satisfy the first law of thermodynamics. The effects of the heat released by combustion and the phase-change energy are accounted for in the description of the absolute enthalpies for various species. In the following, we present the equations for the continuous and the dispersed phases along with a discussion of the numerical treatment of these equations in a homogeneous shear configuration.

2.1. *Continuous phase*

The carrier phase (composed of the oxidizer, the fuel vapour, and the product) is considered to be a compressible and Newtonian fluid with zero bulk viscosity, and to obey the perfect gas equation of state. The instantaneous density, velocity, pressure, and temperature of the carrier phase are denoted by ρ, U_i, P, and T, respectively. The instantaneous mass fractions of the fuel vapour and the oxidizer are denoted by Y_{fv} and Y_{ox}, respectively. With this nomenclature, the Eulerian forms of the non-dimensional continuity, momentum, and energy equations for the carrier phase are given by

$$\frac{\partial \rho}{\partial t} + \frac{\partial}{\partial x_j}(\rho U_j) = \mathscr{S}_m, \tag{2}$$

$$\frac{\partial}{\partial t}(\rho U_i) + \frac{\partial}{\partial x_j}(\rho U_i U_j) = -\frac{\partial P}{\partial x_i} + \frac{2}{Re_f}\frac{\partial}{\partial x_j}\left(S_{ij} - \tfrac{1}{3}\Delta\delta_{ij}\right) + \mathscr{S}_{ui}, \tag{3}$$

$$\frac{\partial E_T}{\partial t} + \frac{\partial}{\partial x_j}[U_j(E_T + P)] = \frac{1}{(\gamma - 1)Re_f Pr M_f^2}\frac{\partial^2 T}{\partial x_j \partial x_j} + \frac{2}{Re_f}\frac{\partial}{\partial x_j}\left[U_i\left(S_{ij} - \tfrac{1}{3}\Delta\delta_{ij}\right)\right] + CeDa\rho^2 Y_{fv} Y_{ox} + \mathscr{S}_e, \tag{4}$$

and the conservation equations for the mass fractions are

$$\frac{\partial}{\partial t}(\rho Y_{fv}) + \frac{\partial}{\partial x_j}(\rho Y_{fv} U_j) = \frac{1}{Re_f Sc}\frac{\partial^2 Y_{fv}}{\partial x_j \partial x_j} - Da\rho^2 Y_{fv} Y_{ox} + \mathscr{S}_m, \tag{5}$$

$$\frac{\partial}{\partial t}(\rho Y_{ox}) + \frac{\partial}{\partial x_j}(\rho Y_{ox} U_j) = \frac{1}{Re_f Sc}\frac{\partial^2 Y_{ox}}{\partial x_j \partial x_j} - rDa\rho^2 Y_{fv} Y_{ox}. \tag{6}$$

The total energy (E_T) is the summation of the sensible internal energy ($\rho C_v T$, where C_v is the specific heat of the carrier phase) and the kinetic energy ($\frac{1}{2}\rho U_i U_i$) of the oxidizer–vapour–product mixture. The equation of state is $P = \rho T/\gamma M_f^2$. In the above equations, $\Delta = U_{j,j}$ is the dilatation ($U_{i,j} = \partial U_i/\partial x_j$), $S_{ij} = \frac{1}{2}(U_{i,j} + U_{j,i})$ is the rate-of-strain tensor, and δ_{ij} is the Kroenecker delta function. All of the variables are normalized by reference length (L_f), density (ρ_f), velocity (U_f), and temperature (T_f) scales. The reference Reynolds and Mach numbers are $Re_f = \rho_f U_f L_f/\mu$ and $M_f = U_f/\sqrt{\gamma R T_f}$, respectively, and the Prandtl and Schmidt numbers are given by $Pr = C_p\mu/\kappa$ and $Sc = \mu/\rho\Gamma$, respectively. In these definitions, the carrier-phase variables μ, κ, C_p, γ, and R are the viscosity, the thermal conductivity, the specific heat, the ratio of the specific heats, and the gas constant, respectively, and Γ is the binary mass diffusivity coefficient. Assuming the same specific heat for the liquid and the vapour, the specific enthalpies for the oxidizer, the liquid, the fuel vapour, and the product are, respectively, $h_{ox} = T$, $h_\ell = T$, $h_{fv} = T + \Lambda$, and $h_p = T + \Omega$. Here,

all the enthalpies are normalized by C_pT_f, $\Lambda = L_v/C_pT_f$ and $\Omega = h_p^f/C_pT_f$ with L_v and h_p^f denoting the latent heat of evaporation and the enthalpy of formation of the product, respectively. Without any loss of generality, it is assumed that the enthalpy of formation of the oxidizer and the fuel vapour is zero with respect to that of the product. In (4)–(6), $Ce = [\Lambda - (1+r)\Omega]/(\gamma - 1)M_f^2$ and $Da = \rho_f L_f K_{fwd}/U_f$ are the heat release coefficient and the Damköhler number, respectively. The total energy equation (4) is derived by assuming unity Lewis number ($Le \equiv Sc/Pr = 1$) (Turns 1996). The coupling of the carrier phase with the droplets is through the terms $\mathscr{S}_m$, $\mathscr{S}_{ui}$, and $\mathscr{S}_e$ which describe the mass, momentum, and energy exchange between the phases, respectively. The formulation of these terms and their calculation from the discrete droplet fields are described in § 2.3.

2.2. *Dispersed phase*

The droplets are allowed to evaporate and are assumed to remain spherical with diameter smaller than the smallest length scale of the turbulence and to exhibit an empirically corrected Stokesian drag force. Both interior motions and rotation of the droplets are neglected. The density of the droplets is considered to be constant and much larger than the density of the carrier phase such that only the inertia, the drag, and the gravity forces are significant to the droplet dynamics. As will be discussed in § 2.3, the numerical methodology used in this study to simulate the homogeneous shear particle-laden flow is only applicable in the absence of gravity; therefore, buoyancy effects are not considered. In addition, the droplet volume fraction is assumed to be small and both droplet–droplet interactions and heat transfer due to radiation are neglected. The droplets are tracked individually in a Lagrangian manner, and the instantaneous droplet position, velocity, temperature, and mass are given by X_i, V_i, T_d, and m_d, respectively. With this nomenclature, the non-dimensional Lagrangian equations describing the droplet dynamics are (Crowe *et al.* 1977)

$$\frac{\mathrm{d}X_i}{\mathrm{d}t} = V_i, \tag{7}$$

$$\frac{\mathrm{d}V_i}{\mathrm{d}t} = \frac{f_1}{\tau_d}(U_i^* - V_i), \tag{8}$$

$$\frac{\mathrm{d}T_d}{\mathrm{d}t} = \frac{f_2}{\tau_d}(T^* - T_d) - \frac{f_3}{\tau_d}(Y_s - Y_{fv}^*), \tag{9}$$

and

$$\frac{\mathrm{d}m_d}{\mathrm{d}t} = -f_4\tau_d^{0.5}(Y_s - Y_{fv}^*), \tag{10}$$

where the superscript $*$ indicates the value of a carrier-phase variable at the droplet location, and Y_s is the vapour mass fraction at the surface of the droplet. It is noted that the droplet equations are not (directly) affected by combustion, which takes place in the carrier phase.

The non-dimensional droplet time constant (for Stokesian drag of a spherical droplet) is $\tau_d = Re_f\rho_d d_d^2/18$, where d_d and ρ_d are the droplet diameter and density, respectively. The droplet variables are normalized using the same reference scales as those used for the carrier-phase variables. The function $f_1 = (1 + 0.15Re_d^{0.687})/(1+B)$ in (8) represents an empirical correction to the Stokes drag due to droplet Reynolds numbers of order unity and larger (Wallis 1969) and is valid for droplet Reynolds numbers $Re_d = Re_f\rho^* d_d|U_i^* - V_i| \leqslant 1000$. The transfer number $B = (T^* - T_d)/\Lambda$ accounts for the evaporation effects, and for non-evaporating droplets $B \equiv 0$. The

droplets are assumed 'lumped', so that there is no temperature variation within each droplet. The first term on the right-hand side of (9) represents the rate of change of the droplet temperature due to convective heat transfer with the carrier phase. The factor $f_2 = Nu/3Pr$ represents a correlation for the convective heat transfer coefficient based on an empirically corrected Nusselt number $[Nu = (2+0.6Re_d^{0.5}Pr^{0.33})/(1+B)]$ (Bird, Stewart & Lightfoot 1960). The second term on the right-hand side of (9) represents the change in the droplet internal energy due to phase change. The correlation $f_3 = \rho^* Sh\Lambda/3Sc$ is a function of an empirically corrected Sherwood number ($Sh = 2 + 0.6Re_d^{0.5}Sc^{0.33}$) (Bird *et al.* 1960). For equivalent molecular weights of the gas and the liquid, the vapour mass fraction at the surface of the droplet is proportional to the partial pressure of the vapour. Using the Clausius–Clapeyron relation, the surface mass fraction is described as

$$Y_s = \frac{P_B}{P} \exp\left[\frac{\gamma\Lambda}{(\gamma-1)T_B}\left(1 - \frac{T_B}{T_d}\right)\right], \tag{11}$$

where T_B is the boiling temperature of the liquid at the pressure P_B. Finally, (10) governs the rate of mass transfer from the droplet due to evaporation, which is a function of the vapour mass fraction difference at the droplet surface, the droplet time constant, and the Sherwood number dependent correlation $f_4 = \pi(18/\rho_d)^{0.5}(\rho^* Sh/Re_f^{1.5}Sc)$.

2.3. *Formulation for homogeneous shear configuration*

To configure a homogeneous shear flow suitable for DNS, a linear mean velocity profile is applied to a zero mean turbulent velocity field. Therefore, the carrier-phase instantaneous velocity is expressed as $U_i = Sx_2\delta_{i1} + u_i$, where u_i is the carrier-phase fluctuating velocity. The magnitude of the imposed shear is given by the amplitude of the mean velocity gradient, $S = \partial\langle U_1\rangle/\partial x_2 = \text{const.}$, where $\langle\ \rangle$ indicates the Eulerian ensemble average over the number of grid points. For homogeneous flows which either start from isotropic initial conditions or develop to become independent of the initial conditions, Blaisdell *et al.* (1991) show that the Favre-average fluctuating quantity is the same as the Reynolds-average one. In this study we indicate the fluctuating quantity with the same notation for both types of averaging; the type of averaging is understood from the context.

In order to employ the Fourier spectral method, periodic boundary conditions must be imposed. This is accomplished by solving the governing equations for fluctuating velocities on a grid which deforms with the mean flow. This transformation has been discussed in detail by Rogallo (1981) and Blaisdell, Mansour & Reynolds (1991) and is only summarized here. A computational (deforming) coordinate system (x_i') is related to the fixed (non-deforming) system through $x_i' = Q_{ij}x_j$ where $Q_{ij} = \delta_{ij} - St\delta_{i1}\delta_{j2}$ is the transformation tensor for the present conditions. Performing the transformation on (2)–(6) and dropping the prime on the coordinates, the governing equations in the transformed coordinates become

$$\frac{\partial\rho}{\partial t} + Q_{ji}\frac{\partial}{\partial x_j}(\rho u_i) = \mathscr{S}_m, \tag{12}$$

$$\frac{\partial}{\partial t}(\rho u_i) + Q_{kj}\frac{\partial}{\partial x_k}(\rho u_i u_j) = -\rho u_2 S\delta_{i1} - Q_{ki}\frac{\partial P}{\partial x_k} + \frac{Q_{kj}}{Re_f}\frac{\partial}{\partial x_k}\left(Q_{ki}\frac{\partial u_j}{\partial x_k} + Q_{kj}\frac{\partial u_i}{\partial x_k} - \tfrac{2}{3}\Lambda\delta_{ij}\right) + \mathscr{S}_{ui}, \tag{13}$$

$$\frac{\partial e_T}{\partial t} + Q_{kj}\frac{\partial}{\partial x_k}[u_j(P+e_T)] = -\rho u_1 u_2 S + \frac{S}{Re_f}\left(Q_{k2}\frac{\partial u_1}{\partial x_k} + Q_{k1}\frac{\partial u_2}{\partial x_k} + S\right) + \frac{Q_{ki}}{Re_f}\frac{\partial}{\partial x_k}\left[u_j\left(Q_{ki}\frac{\partial u_j}{\partial x_k} + Q_{kj}\frac{\partial u_i}{\partial x_k} - \tfrac{2}{3}\Delta\delta_{ij} + S\delta_{i1}\delta_{j2} + S\delta_{i2}\delta_{j1}\right)\right] + \frac{Q_{ki}Q_{ji}}{(\gamma-1)Re_f Pr M_f^2}\frac{\partial^2 T}{\partial x_k \partial x_j} + CeDa\rho^2 Y_{fv} Y_{ox} + \mathscr{S}_e, \tag{14}$$

$$\frac{\partial}{\partial t}(\rho Y_{fv}) + Q_{kj}\frac{\partial}{\partial x_k}(\rho u_j Y_{fv}) = \frac{Q_{ki}Q_{ji}}{Re_f Sc}\frac{\partial^2 Y_{fv}}{\partial x_k \partial x_j} - Da\rho^2 Y_{fv} Y_{ox} + \mathscr{S}_m, \tag{15}$$

$$\frac{\partial}{\partial t}(\rho Y_{ox}) + Q_{kj}\frac{\partial}{\partial x_k}(\rho u_j Y_{ox}) = \frac{Q_{ki}Q_{ji}}{Re_f Sc}\frac{\partial^2 Y_{ox}}{\partial x_k \partial x_j} - rDa\rho^2 Y_{fv} Y_{ox}, \tag{16}$$

where $\Delta = Q_{ji}u_{i,j}$, and $e_T = \rho C_v T + \frac{1}{2}\rho u_i u_i$.

In the absence of gravity or other external body forces and by assuming that the droplets start from the same initial velocities as those of their surrounding fluid elements, the droplet instantaneous velocity is (Simonin, Deutsch & Boivin 1995) $V_i = Sx_2\delta_{i1} + v_i$, with v_i denoting the droplet fluctuating velocity. By performing ensemble averaging on the droplet instantaneous equations, it can be shown that the dispersed phase is homogeneous within the deforming domain used to simulate the carrier phase; thus, periodic boundary conditions can be applied to the dispersed phase as well. The droplet position and momentum equations in the transformed coordinates read

$$\frac{\mathrm{d}X_i}{\mathrm{d}t} = Q_{ik}v_k, \tag{17}$$

$$\frac{\mathrm{d}v_i}{\mathrm{d}t} = \frac{f_1}{\tau_d}(u_i^* - v_i) - v_2 S\delta_{i1}. \tag{18}$$

The equations for the scalar quantities T_d and m_d remain the same as those given by (9) and (10).

The source/sink terms $\mathscr{S}_m$, $\mathscr{S}_{ui}$, and $\mathscr{S}_e$ appearing in (12)–(15) represent the integrated effects of the droplet mass, momentum, and energy exchange with the carrier phase. These Eulerian variables are calculated from the Lagrangian droplet variables by volume averaging the contributions from all of the individual droplets residing within the cell volume ($\delta\mathscr{V} = (\delta x)^3$, where δx is the node spacing) centred around each grid point. In the deforming coordinates, these terms are expressed as

$$\mathscr{S}_m = -\frac{1}{\delta\mathscr{V}}\sum^{n_c}\frac{\mathrm{d}m_d}{\mathrm{d}t}, \tag{19}$$

$$\mathscr{S}_{ui} = -\frac{1}{\delta\mathscr{V}}\sum^{n_c}\left[\frac{m_d f_1}{\tau_d}(u_i^* - v_i) + \frac{\mathrm{d}m_d}{\mathrm{d}t}v_i\right], \tag{20}$$

$$\mathscr{S}_e = -\frac{1}{\delta\mathscr{V}}\sum^{n_c}\left[\frac{1}{(\gamma-1)M_f^2}\frac{\mathrm{d}}{\mathrm{d}t}(m_d T_d) - \frac{\Lambda}{(\gamma-1)M_f^2}\frac{\mathrm{d}m_d}{\mathrm{d}t} + \frac{m_d f_1}{\tau_d}(u_i^* - v_i)v_i + \frac{\mathrm{d}m_d}{\mathrm{d}t}\left(\tfrac{1}{2}v_i v_i\right)\right]. \tag{21}$$

In these equations, n_c is the number of droplets within the cell volume and those cells

Case reference	Coup.	Evap.	Reac.	Φ_{m0}	τ_{d0}	Da	Ce	$N_d \times 10^{-5}$
One-way	1-way	No	No	—	1.0	—	—	1.55
Non-evaporating	2-way	No	No	0.2	1.0	—	—	3.10
Evaporating	2-way	Yes	No	0.2	1.0	—	—	3.10
Base case	**2-way**	**Yes**	**Yes**	**0.2**	**1.0**	**0.5**	**20**	**3.10**
$2\Phi_{m0b}$	2-way	Yes	Yes	0.4	1.0	0.5	20	6.20
$4\Phi_{m0b}$	2-way	Yes	Yes	0.8	1.0	0.5	20	12.40
$0.5\tau_{d0b}$	2-way	Yes	Yes	0.2	0.5	0.5	20	8.77
$0.2Da_b$	2-way	Yes	Yes	0.2	1.0	0.1	20	3.10
$1.5Ce_b$	2-way	Yes	Yes	0.2	1.0	0.5	30	3.10

TABLE 2. Cases considered in the study. For all of the cases $\Lambda = 0.8$, $T_B = 4$, and $r = 1$.

with $n_c = 0$ are assigned a zero value for each variable. A physical interpretation for these source/sink terms may be found in Mashayek (1998*a*).

The computational methodology and the initialization are the same as those employed in Mashayek (1998*a*) and will not be detailed here. All the Eulerian fields are calculated using a pseudospectral method and the Lagrangian droplet equations are integrated using a second-order-accurate Adams–Bashforth method. To evaluate the carrier-phase variables at the droplet location a fourth-order-accurate Lagrange polynomial interpolation scheme is employed. The density and velocity fields are initialized as random Gaussian, isotropic, and solenoidal fields in Fourier space. The initial temperature field has no fluctuations and the initial pressure field is calculated using the equation of state. The initial spectrum, for both density and velocity, has a box-type shape with non-zero and constant value only for $8 < K < 16$ where K is the wavenumber. The droplets are randomly distributed in the flow at $t = 0$ with the same velocity and temperature as those of their surrounding fluid. The initial mean gas density and mean gas temperature are used as the reference scales for density and temperature, respectively. The reference Mach number is $M_f = 1$; therefore, the speed of sound based on the initial mean gas temperature is the reference scale for the velocity. For all of the simulations $Re_f = 500$, $Pr = Sc = 0.7$, $\gamma = 1.4$, $S = 2$, and $\rho_d = 500$.

3. Overview of simulations

The number of parameters involved in the problem is too large to allow a detail investigation of the effects of all of them. Further, the values of the parameters must be chosen carefully such that all the Eulerian fields are resolved accurately and all the assumptions used in the formulation are satisfied. Our previous study of evaporating droplets (Mashayek 1998*a*) and the results of several preliminary simulations (not included here) have been utilized for identifying the appropriate values for various parameters. A listing of all the simulations considered in this study is provided in table 2, with subscript '0' referring to the initial value of a variable at $t = 0$. Here, we consider a 'base case', indicated by boldface in the table, and then change the value of one of the parameters in each of the following simulations. The parameters studied, include the initial mass loading ratio (Φ_{m0}), the initial droplet time constant (τ_{d0}), the Damköhler number (Da), and the heat release coefficient (Ce). Due to the particular importance of the mass loading ratio, we consider two cases with $\Phi_{m0} = 0.4$ and 0.8. The results of the reacting simulations are compared (where necessary) with the data

from non-reacting cases with or without two-way coupling and/or evaporation. The abbreviation used to refer to each case in the presentation of the results is shown in the first column of table 2, where the subscript '*b*' refers to the value of a parameter in the base case. The droplets begin to evaporate (and react in reacting cases) at the normalized time $St = 2$ (S is the magnitude of the mean shear) when the carrier-phase turbulence kinetic energy starts to grow. The condition of one- or two-way coupling, however, is imposed from $t = 0$ for corresponding cases. The number of droplets (N_d) tracked in each case is also shown in the table. For all of the cases, $\Lambda = 0.8$, $T_B = 4$, $r = 1$, and P_B is chosen to be the same as the initial pressure of the oxidizer gas.

The code has been carefully tested by performing the laminar flow test, and by comparisons with the results of the previous work on single-phase compressible flow by Blaisdell *et al.* (1991). The details of these tests are not presented here for brevity. The code has also been previously used by Mashayek (1998*a*) for simulations of non-evaporating and evaporating droplets in the same flow configuration as that considered here. Further evidence for the accuracy of the code may be found in Mashayek (1998*a*) where it is shown that the DNS results accurately satisfy the kinetic and the internal energy equations for both phases. In the simulations, we have considered the highest possible Reynolds number without jeopardizing the small-scale resolution for all of the fields. The flow field (without the presence of the droplets) used for this study has similar characteristics to those simulated by Blaisdell *et al.* (1993) at the same grid resolution and initial r.m.s. turbulence Mach number of 0.2. However, the Reynolds number is smaller in this study as we are dealing with evaporating droplets and so their sizes decrease to small values in time. As the sizes of the droplets decrease they interact with smaller scales of the flow; therefore, it is important to accurately resolve the small scales. All the simulations presented here are performed on 96^3 collocation points with a time step of 2.5×10^{-3}, and are continued till the non-dimensional time $St = 14$. The CPU time (on a CRAY-T90) is 10.5 s per iteration for the reacting case in two-way coupling with 6.2×10^5 droplets. The memory required for this case is 56 Mw.

Before implementing the data generated by the simulations for detailed analysis, it is important to ensure that various fields are sufficiently resolved and that the assumptions invoked in the formulation of the problem are reasonably satisfied. A well-established measure for small-scale resolution of the velocity field is the parameter ηK_{max}, where η is the Kolmogorov length scale and K_{max} is the highest wavenumber resolved in the simulations. The value of ηK_{max} was monitored throughout the simulations and it was always above 1.3 which is sufficiently larger than the (suggested) acceptable limit of unity. The results show that the presence of the droplets results in the increase of ηK_{max}, thus improving the resolution.

To further investigate the resolution at small scales, various spectra are considered for the base case at $St = 14$. Due to the anisotropic nature of the homogeneous shear flow various directional velocity energy spectra must be considered. However, in order to demonstrate the resolution, it suffices to consider the variation of the spectrum with the wavenumber magnitude only. This energy spectrum is shown in figure 1(*a*) and indicates that the cascade of the energy is well established and the energy content decreases with the increase of the wavenumber for large values of K. The peak of the spectrum is around $K = 7$ whereas the highest resolved wavenumber is $K_{max} = 45$. The dissipation spectrum, D_v, in figure 1(*b*) shows that most of the dissipation occurs at higher wavenumbers as expected. The power spectra for the density and the temperature fluctuations of the carrier phase are shown in figure 1(*c*) and (*d*), respectively. These spectra indicate that the thermodynamic fields are also

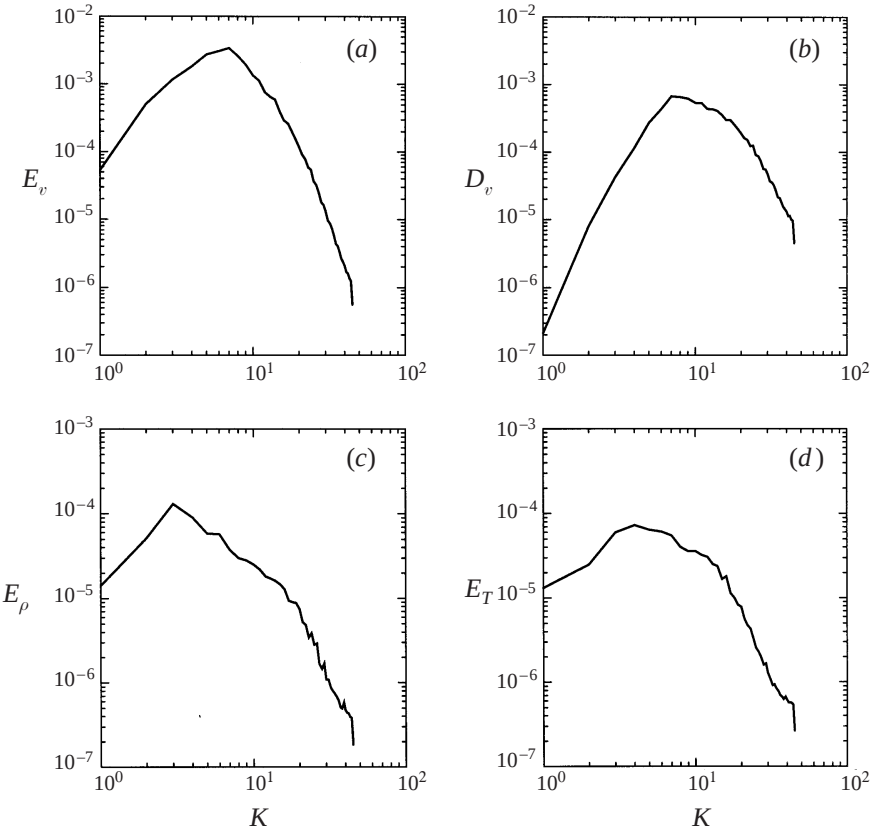

FIGURE 1. Power spectra of (*a*) velocity, (*b*) dissipation, (*c*) density, and (*d*) temperature of the carrier phase for the base case at $St = 14$.

resolved satisfactorily and there is no increase of the energy at high wavenumbers. Further inspections of various spectra at other times and for other simulations also indicated acceptable accuracy in resolving the small scales.

Next, we consider various spectra for the other two simulated Eulerian fields, i.e. the mass fractions of the fuel vapour and the oxidizer. The resolution of the fuel vapour mass fraction is particularly important as the droplets, which are the source of the fuel vapour, are not uniformly distributed within the simulation domain due to the effects of the preferential concentration. In figure 2(*a*) and (*c*) the spectra of the fluctuations of the fuel vapour mass fraction at various times are shown for cases without and with chemical reaction at $\Phi_{m0} = 0.2$, respectively. The droplets begin to evaporate at $St = 2$ and, as expected, figure 2 indicates that during the early stages ($St = 2.2$) most of the energy is concentrated at high wavenumbers. However, the situation is improved rapidly such that at $St = 3$ the peak of the spectra has moved to $K \simeq 15$. At long times, the peak of the spectra is around $K \simeq 8$. It is important to note that, except for a very short time after the onset of evaporation, no increase of energy at high wavenumbers is observed. The spectra in figure 2(*a*) and (*c*) indicate that there could still be some room for further improvement of the resolution; however, the resolution achieved is reasonably acceptable as there is enough separation between the peak wavenumber and K_{max}. Similar spectra are shown in figure 2(*b*) and (*d*) for the fluctuations of the oxidizer mass fraction. As expected, these spectra exhibit higher resolution throughout the simulation and, again, there is no increase of energy

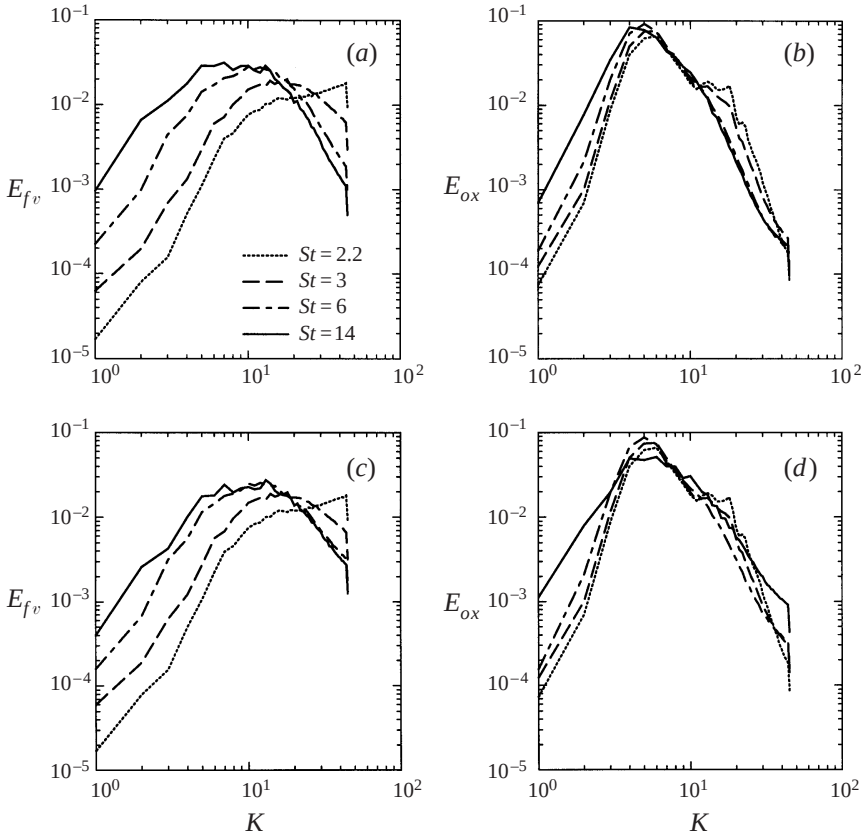

FIGURE 2. Temporal evolution of the spectra of the fuel vapour mass fraction in (*a*) and (*c*), and the oxidizer mass fraction in (*b*) and (*d*): (*c*, *d*) for the base case, and (*a*, *b*) for the respective evaporating (non-reacting) case.

at high wavenumbers. The effect of the fuel vapour on the oxidizer during the early stages of evaporation is evident from the local increase in the spectrum of the oxidizer at $St = 2.2$. This local peak, around $K \simeq 17$, corresponds to the high-energy portion of the fuel vapour spectrum at $St = 2.2$. It is also noted, at $St = 14$, that for reacting droplets the spectra of the fuel vapour and the oxidizer are more similar as compared to those in the evaporating case. This suggests that reaction tends to diminish the structural differences between the fuel vapour and the oxidizer. Further evidence for this observation is provided in §4 where we analyse the evolution of the Taylor microscale for these fields.

The assumption of Stokesian drag requires droplet sizes smaller than the smallest scales of the turbulence such that the flow field around each droplet can be considered homogeneous. At the same time, however, the size of the droplet must be much larger than the mean free path of the molecules of the carrier phase in order to consider a continuum around the droplet. Referring to an analysis by Lumley (1978), Elghobashi & Truesdell (1992) argue that the use of the Stokes approximation for the motion of a single droplet is justified if $d_d/\eta < \frac{1}{6}$ and $Re_d < 0.5$. Figure 3 shows that $\langle\langle Re_d \rangle\rangle$ (the notation $\langle\langle\ \rangle\rangle$ indicates the Lagrangian ensemble average over the number of droplets) is less than ~ 0.6 throughout the simulations and closely satisfies the criterion. The droplet Reynolds number starts from zero (as a result of the imposed initial condition)

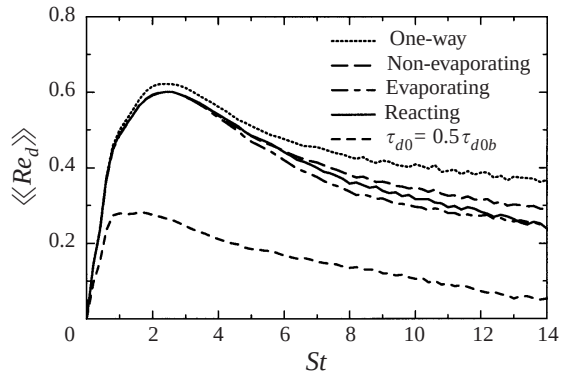

FIGURE 3. Temporal variation of the Lagrangian-average droplet Reynolds number.

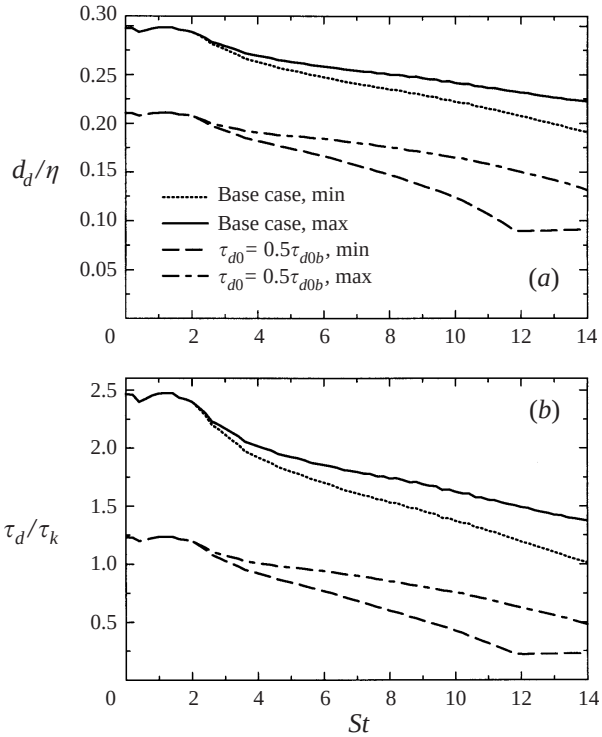

FIGURE 4. Temporal variation of the minimum and maximum values of (*a*) the droplet diameter normalized by the Kolmogorov length scale and (*b*) the droplet time constant normalized by the Kolmogorov time scale.

and reaches a peak value around $St = 2$. It is suggested in the literature (e.g. Riley & Patterson 1974; Elghobashi & Truesdell 1992) that after the peak time the effects of the initial conditions are significantly diminished and the results may be used for statistical analysis. This is another reason for allowing the droplets to evaporate (and react) at and after $St = 2$ in these simulations.

The temporal variation of the minimum and maximum values of d_d/η is portrayed in figure 4(*a*) for two reacting cases. It is observed that the value of d_d/η for the base case also closely satisfies the above condition. For the case with smaller droplets,

however, d_d/η falls slightly below the suggested value of $\frac{1}{6}$ towards the end of the simulation. To avoid very small droplets, a criterion was set in the code to remove the droplets when their diameters fall below a certain value. These droplets are not replaced and do not participate in the calculation of the dispersed-phase statistics. Figure 4(*a*) clearly shows that, for the case with $\tau_{d0} = 0.5\tau_{d0b}$, the minimum value of d_d/η does not change after $St = 12$ as a result of the application of the above criterion for the minimum droplet size. Previous studies (e.g. Wang & Maxey 1993) show that the effects of the preferential distribution are enhanced for droplet time constants of the order of the Kolmogorov time scale, τ_k. This has been the primary criterion for choosing the initial values of the droplet time constant for this study. Figure 4(*b*) shows that $0.24 < \tau_d/\tau_k < 2.46$ for these simulations.

Other statistics of the two-phase flow have also been carefully examined for the assessment of the accuracy of the generated data. The analysis of the results indicated that the mean turbulent Mach number is always less than 0.2 and the flow is free of shocklets. The value of the integral length scale was also monitored for all the simulations and never exceeded 6% of the size of the simulation box. This indicates that the simulated flow remains homogeneous for all of the cases.

4. Droplet size, fuel vapour, and oxidizer

In this section, the droplet size distribution and mass fractions of the fuel vapour and oxidizer are investigated. Since all of these quantities depend on the amount of the evaporated mass, it is instructive to first consider the variations of the Lagrangian average mass of the droplets. The temporal variation of this quantity, normalized by its initial value, is shown in figure 5(*a*) for various cases. It is observed that the evaporation rate decreases with the increase of the mass loading ratio, as a result of the increase in the total mass of the vapour in the carrier phase. The decrease of the droplet time constant, however, enhances the evaporation rate due to the increase in the surface area to volume ratio. Note that, during the final stages of the simulation with $\tau_{d0} = 0.5\tau_{d0b}$, the rate of evaporation decreases abruptly. As was discussed in § 3, this is due to the fact that some of the droplets are fully (within the set criterion) evaporated and are removed from the simulation. Figure 5(*a*) also shows that the decrease of either the Damköhler number or the heat release coefficient decreases the rate of evaporation as a result of a decrease in the energy released by combustion. In all of the cases, a portion of the evaporated mass participates in the chemical reaction with the oxidizer. Figure 5(*b*) shows the temporal variation of the remaining (unburnt) mass of the fuel vapour, m_{fv}, divided by the total evaporated mass. It is noted that the ratio decreases as the reaction proceeds for all of the cases. However, this should not imply that the mean fuel vapour mass fraction also decreases in time; variations of $\langle Y_{fv} \rangle$ will be discussed later in this section. It is interesting that, despite the large variations in the evaporation rate, as noted in figure 5(*a*), the quantity $\langle m_{fv} \rangle / \langle \langle m_{d0} - m_d \rangle \rangle$ remains closely the same for all of the cases but that with small Damköhler number.

The modelling of spray combustion often involves an approximation for the size of the droplets. One approach is to describe the droplet size distribution by known probability density functions (p.d.f.s). The droplet size distribution is investigated here by considering the temporal variation of various moments shown in figure 6. These moments along with the mean droplet size, obtained from figure 5(*a*), can be used to approximate the p.d.f. of the droplet size at various times. A close inspection of figure 6(*a*) shows that with the progress of the chemical reaction the normalized root

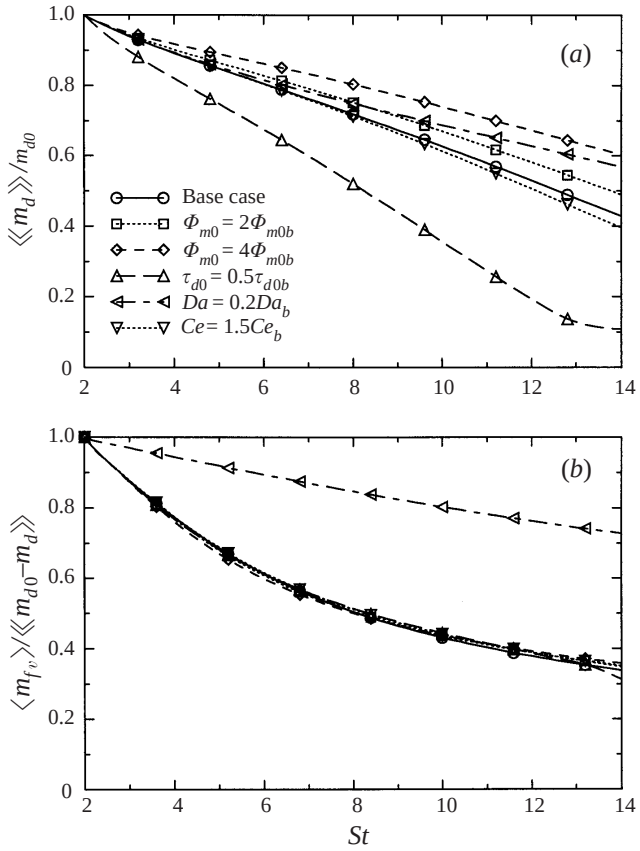

FIGURE 5. Temporal variation of (*a*) the mass of the droplets normalized with its initial value and (*b*) the remaining mass of the fuel vapour normalized with the total evaporated mass.

mean square (r.m.s.) of the droplet diameter, d_{drms}/d_{d0}, increases in time for all of the cases. The skewness and kurtosis values in figure 6(*b*) suggest that the long time distribution of the droplet size may be closely approximated with a Gaussian p.d.f. for all of the cases. The increase of the mass loading ratio increases the r.m.s. of the droplet diameter while shifting its skewness from positive to negative at long times. The decrease of the initial droplet size also significantly increases the r.m.s., in agreement to the results shown in figure 4(*a*) which indicate a larger difference between the minimum and maximum values of the droplet diameter in the case with $\tau_{d0} = 0.5\tau_{d0b}$. Changes in either the Damköhler number or the heat release coefficient appear to have little effect on the droplet size distribution.

In order to study the droplet size distribution in connection with various Eulerian fields, it is necessary to provide a Eulerian description for the density of the droplets. For non-evaporating droplets (or solid particles) it is customary (e.g. Squires & Eaton 1991*b*) to use the 'droplet number density', n_d, calculated in a manner similar to that used for the source term in the carrier-phase equations; i.e. n_d is defined as the number of droplets within the cell surrounding each Eulerian grid point. This definition does not carry any information on the mass of the droplets. Therefore, for evaporating (and reacting) droplets we also introduce the 'droplet Eulerian density', $C_d = \sum^{n_d} m_d/\rho\delta\mathscr{V}$ which accounts for the mass of the droplets. Note that C_d is normalized such that it

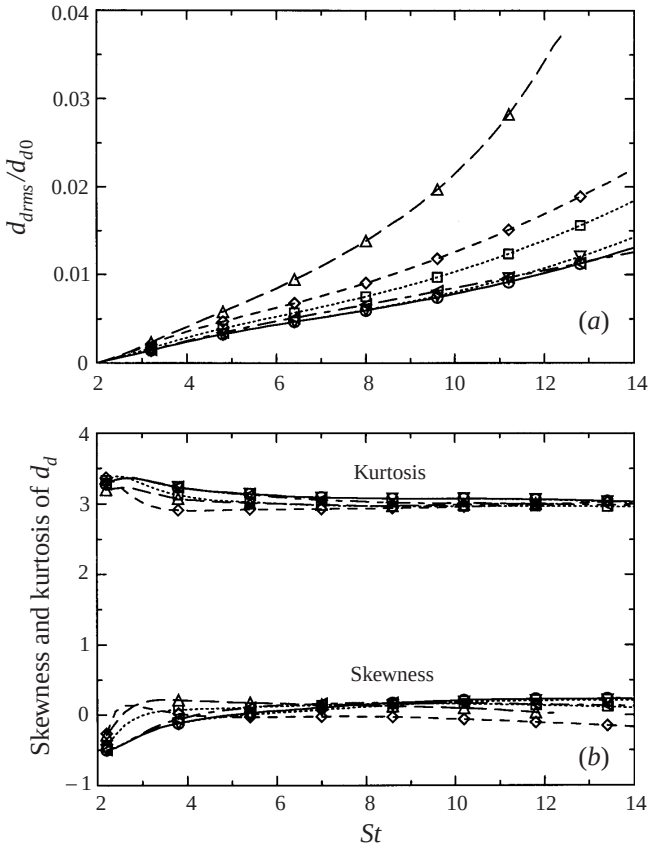

FIGURE 6. Temporal variation of (*a*) r.m.s. and (*b*) skewness and kurtosis of the droplet diameter. Symbols as figure 5.

describes the ratio of the total mass of the droplets to the mass of the carrier phase within a cell. Therefore, C_d may also be interpreted as a Eulerian description for the mass loading ratio. The relationship between the droplet number density and the droplet Eulerian density can be investigated by considering their joint p.d.f. in figure 7 for the case with the highest mass loading ratio ($\Phi_{m0} = 4\Phi_{m0b}$) at $St = 14$. A similar behaviour was observed for other cases. The high peak of the p.d.f. at the origin indicates that a large portion of the domain is free of droplets. This is due mainly to the preferrential accumulation of the droplets in high strain rate regions of the flow as shown previously (Wang & Maxey 1993; Eaton & Fessler 1994) and will also be addressed in § 5. As one would expect, figure 7 indicates that the probability of finding one droplet per cell is larger than that of finding two or more droplets per cell.

We begin our discussion on the reactants by considering the joint p.d.f.s of the fuel vapour mass fraction with the droplet number density and the droplet Eulerian density as the droplets are the source for the fuel vapour. These p.d.f.s, shown in figure 8 for the case with the highest mass loading ratio, indicate the existence of a considerable probability of finding fuel vapour in the regions of the flow that do not contain any droplet. This can be an indication that the diffusion time for the fuel vapour is relatively small or that the time scale for the motion of the droplets is small enough, compared to the time scale of reaction, such that before the fuel vapour is

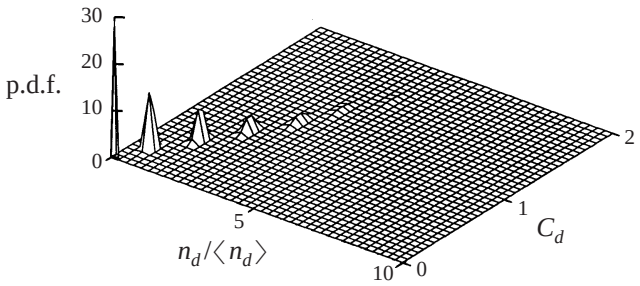

FIGURE 7. Joint p.d.f. of (*a*) the droplet number density (n_d) and (*b*) the droplet Eulerian density (C_d) for the case with $\Phi_{m0} = 4\Phi_{m0b}$ at $St = 14$.

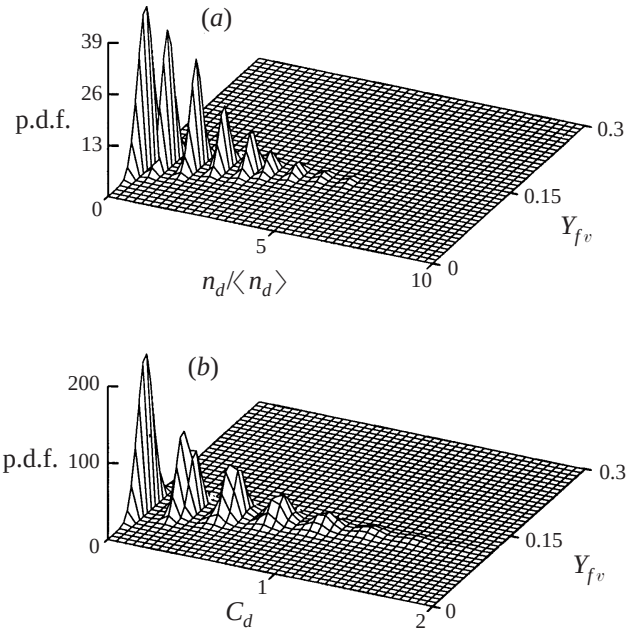

FIGURE 8. Joint p.d.f. of the fuel vapour mass fraction and the droplet number density in (*a*), and the droplet Eulerian density in (*b*), for the case with $\Phi_{m0} = 4\Phi_{m0b}$ at $St = 14$.

completely consumed by reaction some of the droplets have left the region. These hypotheses gain some support from the relatively small values used for the Scmidt number and the Damköhler number, and from figure 4(*b*) which shows that the droplet time constant is of the same order of magnitude as that of the smallest scales of the turbulence. Nevertheless, a close inspection of figure 8 reveals that the peak of the p.d.f. moves towards smaller values of Y_{fv} as n_d (or C_d) decreases. Therefore, the total amount of the fuel vapour in the droplet-free regions of the flow must be somewhat small in comparison to that in the regions occupied by the droplets. Figure 8 also shows that the p.d.f. is more diffused along the C_d-axis compared to the n_d-axis and the relative height of the p.d.f. in the droplet-free regions of the flow increases when the joint p.d.f. with C_d is considered.

The reaction rate strongly depends on the correlation between the mass fractions of the fuel vapour and the oxidizer, and an effective means for increasing the rate of reaction is by improving the mixing of the two species. The issue of mixing can

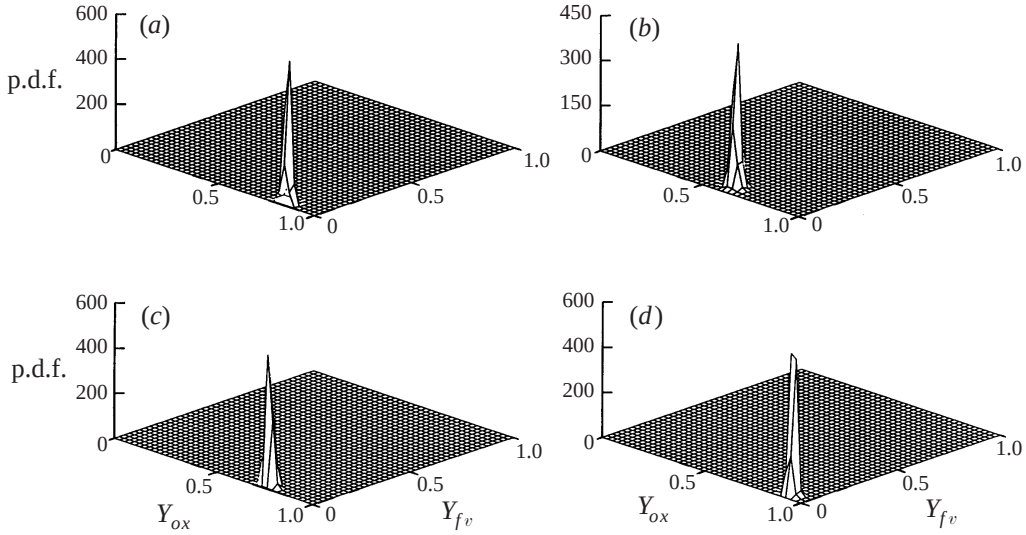

FIGURE 9. Joint p.d.f. of the fuel vapour and oxidizer mass fractions for (*a*) the base case, (*b*) $\Phi_{m0} = 4\Phi_{m0b}$, (*c*) $\tau_{d0} = 0.5\tau_{d0b}$, and (*d*) $Da = 0.2Da_b$, at $St = 14$.

be investigated by considering the joint p.d.f. of the mass fractions. In non-premixed reaction, where species are initially segregated, the joint p.d.f. is represented by two seperate peaks. Previous investigations in single-phase flows (e.g. McMurtry & Givi 1989) indicate that turbulence motions are capable of enhancing the rate of mixing significantly such that the joint p.d.f. evolves into a single-peak p.d.f. at which point the species are considered to be mixed. The joint p.d.f.s of Y_{fv} and Y_{ox} are shown in figure 9 for various cases at $St = 14$. A comparison of these p.d.f.s with those found in the literature for premixed reaction (in single-phase flow) suggests that the fuel vapour and the oxidizer are well mixed at this stage and the reaction may be categorized as premixed. It is noted that the joint p.d.f. is concentrated in the small-Y_{fv} region as the amount of the vapour in the carrier phase is small in comparison to the mass of the oxidizer (and the product). The joint p.d.f. moves towards smaller values of Y_{ox} when the mass loading ratio is increased (figure 9*b*) or the droplet time constant is decreased (figure 9*c*). An opposite effect is observed with the decrease of the Damköhler number. It is also noted that the p.d.f. moves towards larger values of Y_{fv} with the increase of the mass loading ratio. This could indicate that the rate of production of the fuel vapour by evaporation is larger than its rate of consumption by reaction. This issue can be further investigated by considering the evolution of the mean fuel vapour mass fraction.

Figure 10 portrays the temporal variations of the mean fuel vapour mass fraction and the mean oxidizer mass fraction. The general observation is that the mean mass fraction of the fuel vapour increases in time whereas, as expected, the mean oxidizer mass fraction decreases. An exception is the case with smaller droplet time constant which shows a decreasing trend for $\langle Y_{fv} \rangle$ at the end of the simulation. As was pointed out earlier, this is due to the fact that most of the droplets are evaporated at this stage and do not contribute to the production of the fuel vapour. The increase of $\langle Y_{fv} \rangle$ is despite the consumption of the fuel vapour by reaction, and indicates that the rate of production is larger than the rate of consumption of the vapour. It must be emphasized that the variation of the fuel vapour mass fraction strongly depends

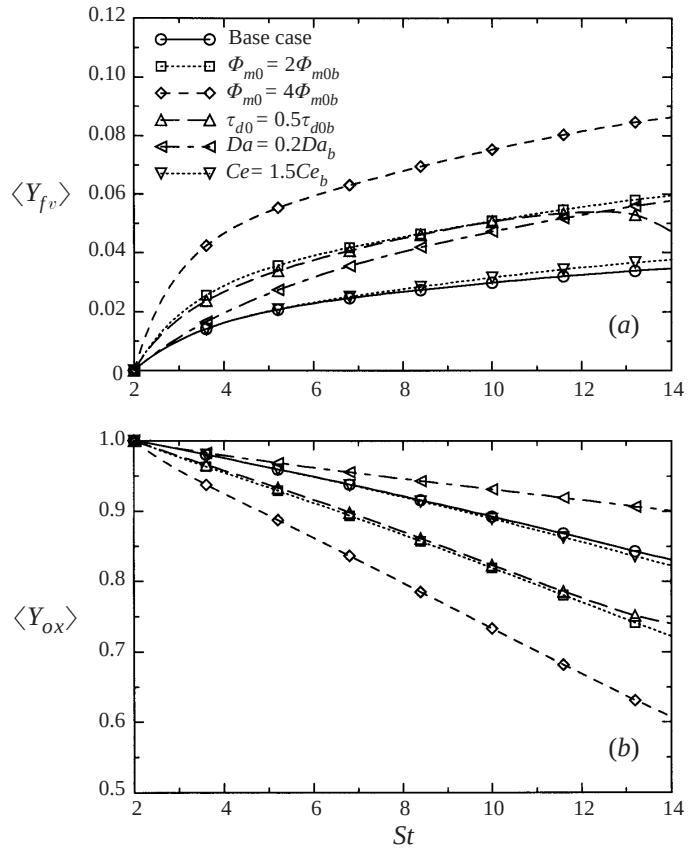

FIGURE 10. Temporal variation of the mean mass fraction of (*a*) the fuel vapour and (*b*) the oxidizer.

on the values used for various parameters. Nevertheless, it is interesting to note that the temporal variation of $\langle Y_{fv} \rangle$ and $\langle Y_{ox} \rangle$ is nearly linear at long times (again with the exception of the case with $\tau_{d0} = 0.5\tau_{d0b}$). Figure 10(*a*) indicates that either the increase of the mass loading ratio or the decrease of the droplet time constant results in the increase (decrease) of the fuel vapour (oxidizer) mass fraction at all times. By decreasing the reaction rate, the decrease of Da results in the increase of the fuel vapour mass fraction despite the smaller rate of evaporation. Finally, an increase of the heat release coefficient by 50% does not seem to have a significant effect on the mean mass fraction of either reactant.

The temporal evolution of the r.m.s. of the mass fractions, $Y_{fvrms} = [\langle (Y_{fv} - \langle Y_{fv} \rangle)^2 \rangle]^{1/2}$ and $Y_{oxrms} = [\langle (Y_{ox} - \langle Y_{ox} \rangle)^2 \rangle]^{1/2}$, is shown in figure 11. It is clear that Y_{fvrms} is much more sensitive to various parameters than is Y_{oxrms}. The r.m.s. of the vapour mass fraction rapidly increases during the early times as the evaporation rate is initially large and results in the increase of the fuel vapour mass fraction near the droplets. Since the droplets are not uniformly distributed, Y_{fvrms} starts to increase during the early stages of evaporation. This is also due to the fact that the reaction zone (see § 5) is not spatially uniform and results in a non-uniform consumption of the fuel vapour. At long times, turbulent motions distribute the fuel vapour more evenly in space and result in a smaller rate of increase for Y_{fvrms}. The increase of

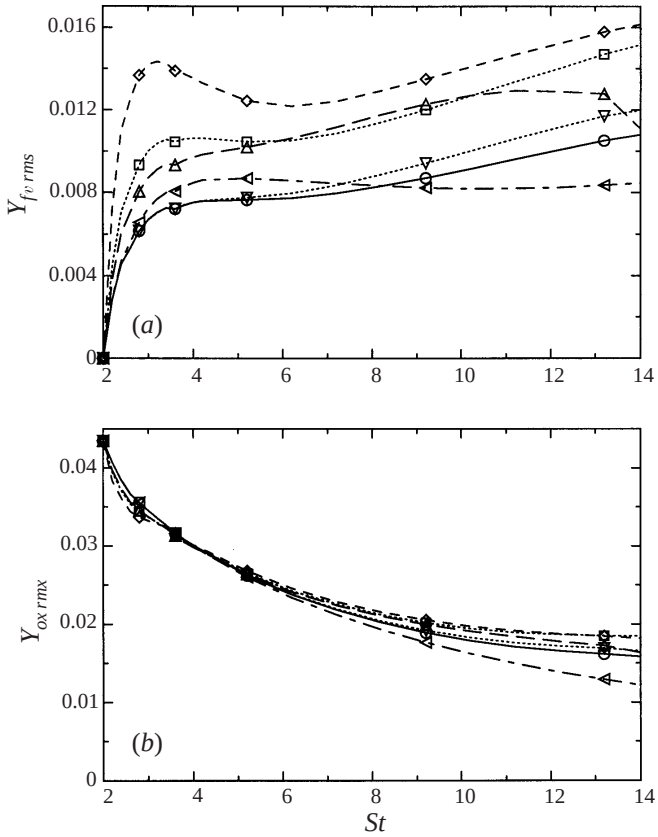

FIGURE 11. Temporal variation of the r.m.s. of the mass fraction of (*a*) the fuel vapour and (*b*) the oxidizer. Symbols as figure 10.

the mass loading ratio increases Y_{fvrms} and causes an overshoot after the initial rapid increase. It is interesting to note that Y_{oxrms} always decreases in time even when Y_{fvrms} is increasing.

To analyse the p.d.f.s of the mass fractions, in figure 12 we consider the skewness and kurtosis of these variables. This analysis could be of great interest in the modelling of the mass fractions during a combustion process. The skewness and kurtosis are calculated for the Reynolds-average fluctuating component of the mass fractions, $Y'_{fv} = Y_{fv} - \langle Y_{fv} \rangle$ and $Y'_{ox} = Y_{ox} - \langle Y_{ox} \rangle$. Figure 12(*a*) shows that during the early stages of evaporation and reaction the skewness and kurtosis values of the fuel vapour mass fraction significantly deviate from those for a Guassian p.d.f. However, these values become close to those of a Gaussian distribution within a short time, as a result of the turbulent motions of the carrier phase. This behaviour is in agreement with the evolution of the power spectra of Y'_{fv} in figure 2. The increase of the mass loading ratio decreases the skewness such that there is a higher probability for finding fuel vapour mass fractions smaller than the mean for the case with $\Phi_{m0} = 4\Phi_{m0b}$. Figure 12(*b*) indicates that the skewness and kurtosis of the oxidizer mass fraction are not influenced by the presence of the fuel vapour and remain very close to those for a Gaussian p.d.f during the early stages of evaporation and reaction for all of the cases. At long times, however, it appears that the oxidizer is significantly affected by the chemical reaction and the kurtosis values increase with either the increase of the

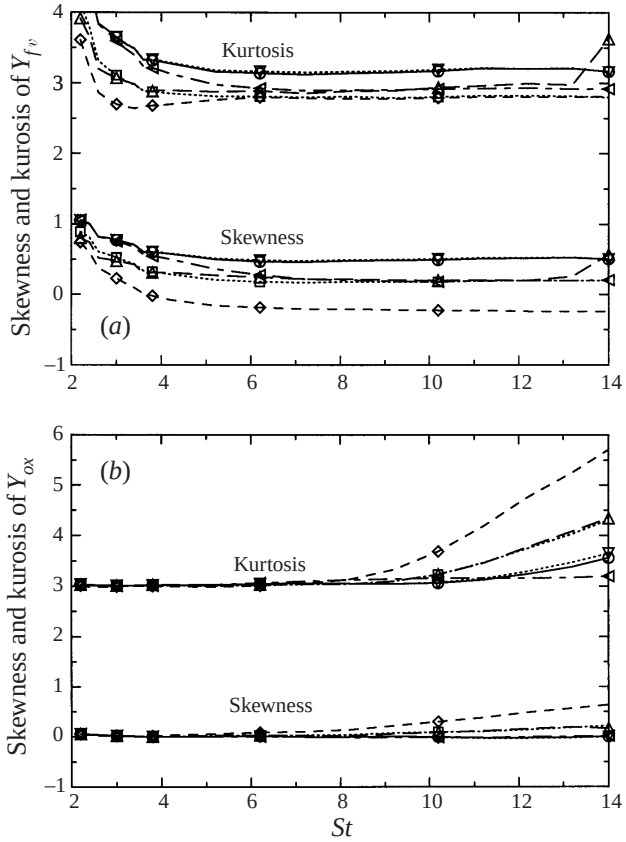

FIGURE 12. Skewness and kurtosis of (*a*) the fuel vapour and (*b*) the oxidizer mass fractions. Symbols as figure 10.

mass loading ratio or the decrease of the droplet time constant. It is not clear from these simulations how the p.d.f.s of the oxidizer mass fraction will behave at longer times ($St > 14$). However, it appears that with the presence of a sustained chemical reaction the p.d.f.s of the oxidizer mass fraction cannot be approximated by a specific type of distribution.

More insight into the turbulence structure of the reactants is gained by studying the temporal evolution of the Taylor microscale λ_{fv} and λ_{ox}, and the small-scale dissipation ϵ_{fv} and ϵ_{ox} for the fuel vapour and the oxidizer mass fractions, respectively, in figure 13. The microscales are defined as $\lambda_{fv} = [12Y_{fv}'^2/(Re_f Sc\epsilon_{fv})]^{1/2}$ and $\lambda_{ox} = [12Y_{ox}'^2/(Re_f Sc\epsilon_{ox})]^{1/2}$, similarly to the microscale for a scalar (Leonard & Hill 1991), and are normalized with the length of the simulation domain, 2π. The results in figure 13(*a*) suggest that the mass fraction fields are mainly composed of small-scale structures compared to the size of the domain. The microscale of the fuel vapour is smaller than that of the oxidizer throughout the simulations. However, figure 13(*a*) shows that chemical reaction results in the decrease of the Taylor microscale for both species, although the impact is much larger on the oxidizer. It may be concluded from the results in figure 13(*a*) that chemical reaction tends to modify the turbulence structure of the oxidizer such that the microscales of the two species become closer.

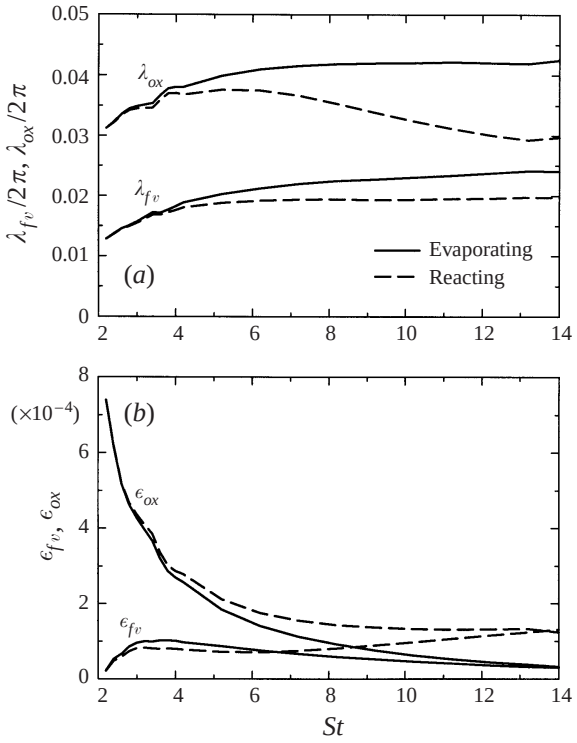

FIGURE 13. Temporal variation of (*a*) the Taylor microscale and (*b*) the dissipation rate of the fuel vapour and the oxidizer mass fractions for the base case and its respective evaporating (non-reacting) case.

The temporal evolution of

$$\epsilon_{fv} = \frac{2}{Re_f Sc}\left\langle \frac{\partial Y'_{fv}}{\partial x_i}\frac{\partial Y'_{fv}}{\partial x_i}\right\rangle, \qquad \epsilon_{ox} = \frac{2}{Re_f Sc}\left\langle \frac{\partial Y'_{ox}}{\partial x_i}\frac{\partial Y'_{ox}}{\partial x_i}\right\rangle$$

is shown in figure 13(*b*). For the non-reacting case, the dissipation rate decreases to the same small value for both species at long times. The chemical reaction, however, results in the increase of the dissipation rate of the fuel vapour mass fraction at long times. This is due mainly to the increase of the fluctuations of the fuel vapour mass fraction which results in a larger energy transfer from high-energy scales to small scales where dissipation occurs.

A convenient approach usually adopted for theoretical analysis of reaction is via the concept of the 'mixture fraction' defined as (Bilger 1980)

$$\xi = \frac{rY_{fv} - Y_{ox} + 1}{1 + r}. \tag{22}$$

In single-phase flows, without any production of fuel or oxidizer, ξ behaves like a 'conserved scalar' as there is no source term in its transport equation. For the present case, however, ξ as defined by (22) is not conserved and increases with time as witnessed from figure 14. To explain the behaviour observed in the figure, a transport equation is derived for ξ using (2), (5), and (6). For homogeneous shear flow and in

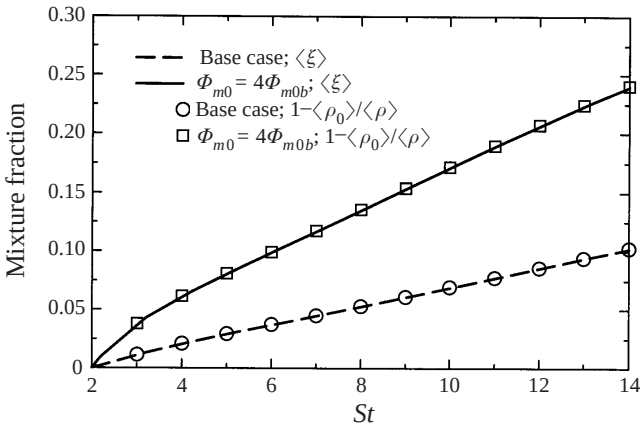

FIGURE 14. Temporal evolution of the mean mixture fraction.

deforming coordinates, this transport equation reads

$$\frac{\partial}{\partial t}(\rho\xi) + Q_{ji}\frac{\partial}{\partial x_j}(\rho u_i \xi) = \frac{Q_{ij}Q_{kj}}{Re_f Sc}\frac{\partial^2 \xi}{\partial x_i \partial x_k} + \mathscr{S}_m. \tag{23}$$

Equation (23) resembles the equation for a conserved scalar except for the droplet mass source term, $\mathscr{S}_m$. With droplets evaporating, this term is always positive and results in the increase of ξ, in agreement to the results in figure 14.

For homogeneous flows, a relationship between the mean value of ξ and the mean carrier-phase density may be obtained by averaging (23). After some algebraic manipulations and by assuming that $\langle\rho\xi\rangle \simeq \langle\rho\rangle\langle\xi\rangle$, the following relation is obtained:

$$\langle\xi\rangle \simeq \frac{\langle\rho\rangle - \langle\rho_0\rangle}{\langle\rho\rangle}, \tag{24}$$

where ρ_0 is the initial value of the carrier-phase density. Figure 14 shows that (24) is in agreement with the results of the numerical simulations. For an infinitely fast reaction with $r = 1$, (22) yields the stoichiometric value $\xi = 0.5$. Figure 14 indicates that the average value of ξ increases in time since the total evaporated mass of the fuel increases; however, it never reaches 0.5 as the initial mass loading ratio is smaller than unity. The maximum of ξ was monitored for all the reacting cases and indicated values less than 0.5 for all times.

5. Reaction rate and zone

The results presented in §4 indicate that in analysing the DNS results special attention must be paid to various mechanisms influencing the mixing of the fuel vapour and the oxidizer. The extensive previous studies conducted on single-phase turbulent reacting flows have revealed the important role of turbulence mixing in enhancing the rate of reaction. In two-phase reacting flows, the dispersion of the droplets may also be considered as an effective means for improving and/or controlling the mixing process. The most important issue in this consideration is the preferential distribution of the droplets (Wang & Maxey 1993; Eaton & Fessler 1994) and the influence of the large scales of the flow on the motion of the droplets. These aspects of the two-phase turbulent reacting flow are explored in this section via statistical

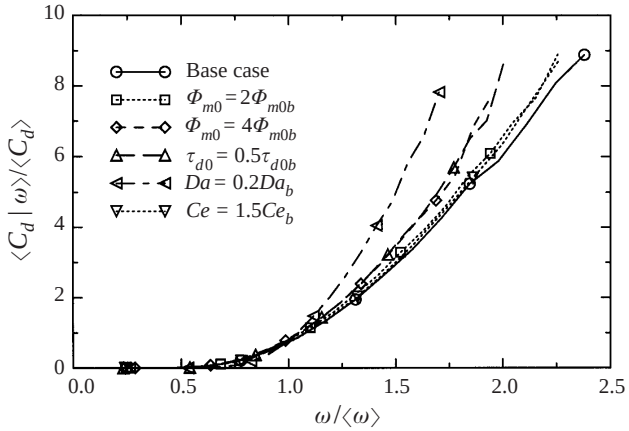

FIGURE 15. Expected value of the droplet Eulerian density conditioned on the reaction rate: $\tau_{d0} = 0.5\tau_{d0b}$ at $St = 12$, all other cases at $St = 14$.

analysis. The primary focus of the investigation, however, is on the reaction rate and reaction zone due to their significance in the modelling of reacting systems.

Figure 15 portrays the variations of the normalized conditional expectation $\langle C_d|\omega\rangle/\langle C_d\rangle$ with $\omega/\langle\omega\rangle$, where $\omega = \rho^2 Da Y_{fv} Y_{ox}$ is the reaction rate. All of the results are at $St = 14$ except for the case with $\tau_{d0} = 0.5\tau_{d0b}$ which is presented at $St = 12$. It is clearly seen in the figure that the regions of high reaction rate are associated with the regions of high droplet concentration. This is due mainly to the fact that droplets are the source for the fuel vapour. Since the initial mass loading ratio for these simulations is less than unity while the stoichiometric coefficient is $r = 1$, the possibility of encountering fuel-rich regions must be small. Therefore, the fuel vapour receives enough oxidizer immediately after leaving the droplet and reaction starts in the neighbourhood of the droplet. For mass loading ratios significantly higher than unity, the correlation between the reaction rate and the droplet concentration could be expected to be smaller. However, for the present cases $\Phi_{m0} \leqslant 0.8$ and figure 15 shows that the expected value of C_d conditioned with the reaction rate increases with the increase of the mass loading ratio. This may be explained by noting from figure 5 that an increase of the mass loading ratio is accompanied by a decrease in the average mass evaporated by each droplet. Further, the increase of Φ_{m0} results in a more uniformly distributed fuel vapour due to the presence of a larger number of droplets. This increases the possibility of finding enough oxidizer in the vicinity of the droplets and facilitates the chemical reaction. For similar reasons the decrease of the droplet time constant also results in the increase of $\langle C_d|\omega\rangle/\langle C_d\rangle$. Figure 15 also shows a substantial increase in the expected value of C_d with the decrease of the Damköhler number, despite the fact that smaller values of the Damköhler number correspond to a slower reaction and combustion may continue after the droplets have left the region. This again has to do with the decrease of the average mass evaporated by each droplet when the Damköhler number is decreased. Finally, it appears from the figure that the increase of the heat release coefficient by 50% does not significantly affect the expected value of C_d.

The effect of the small scales of the flow on the reaction rate is considered next. A

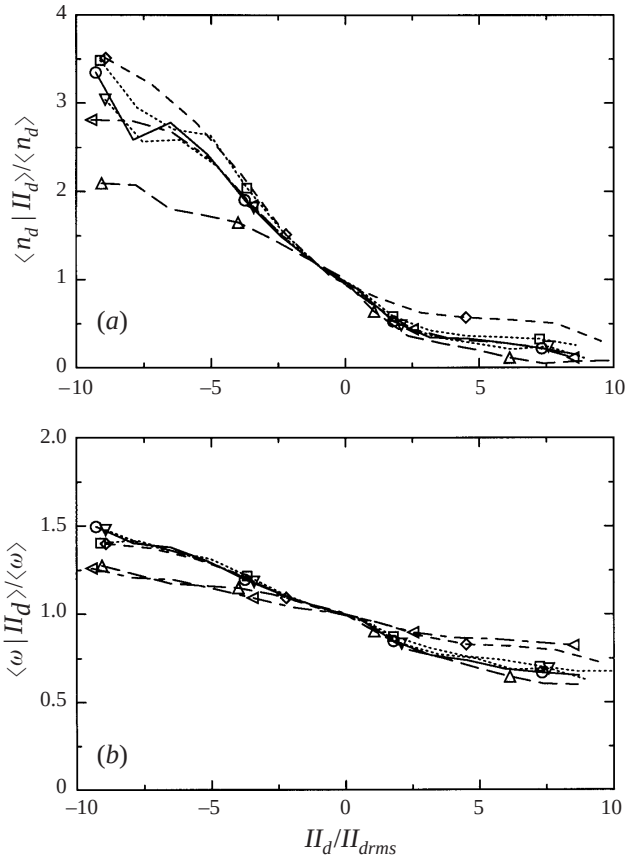

FIGURE 16. Expected value of (*a*) the droplet number density and (*b*) the reaction rate conditioned on II_d: $\tau_{d0} = 0.5\tau_{d0b}$ at $St = 12$, all other cases at $St = 14$. Symbols as figure 15.

convenient parameter for distinguishing various regions in the flow is

$$II_d \equiv -\frac{1}{2}\left(\frac{\partial u_i}{\partial x_j}\frac{\partial u_j}{\partial x_i}\right) = -\tfrac{1}{2}\left(\zeta^2 - \tfrac{1}{4}\vartheta_i\vartheta_i\right), \tag{25}$$

where ζ^2 denotes the magnitude of the strain-rate tensor. In incompressible flows, II_d represents the second invariant of the deformation tensor, $\partial u_i/\partial x_j$ (see e.g. Squires & Eaton 1990). As pointed out by Mashayek (1998*a*), for a compressible flow, II_d does not have an analogous physical significance; however, it may still be used for flow characterization as the negative and positive values of II_d correspond to high-strain-rate and high-vorticity regions of the flow, respectively. It must be emphasized that the parameter II_d is defined based on fluctuating velocities, and does not take into account the large-scale motions due to mean shear. The effect of the mean shear on the reaction zone is discussed later in this section.

Figure 16 shows the variation of $\langle n_d|II_d\rangle/\langle n_d\rangle$ and $\langle\omega|II_d\rangle/\langle\omega\rangle$ with II_d/II_{drms} for various cases. Again, all of the results are at $St = 14$ except for the case with $\tau_{d0} = 0.5\tau_{d0b}$ which is considered at $St = 12$. Similarly to previous observations in incompressible flows laden with solid particles, figure 16(*a*) shows that the droplets exhibit a tendency for accumulating in high-strain-rate (negative II_d) regions of the flow. The previous studies have also shown that the preferential distribution depends

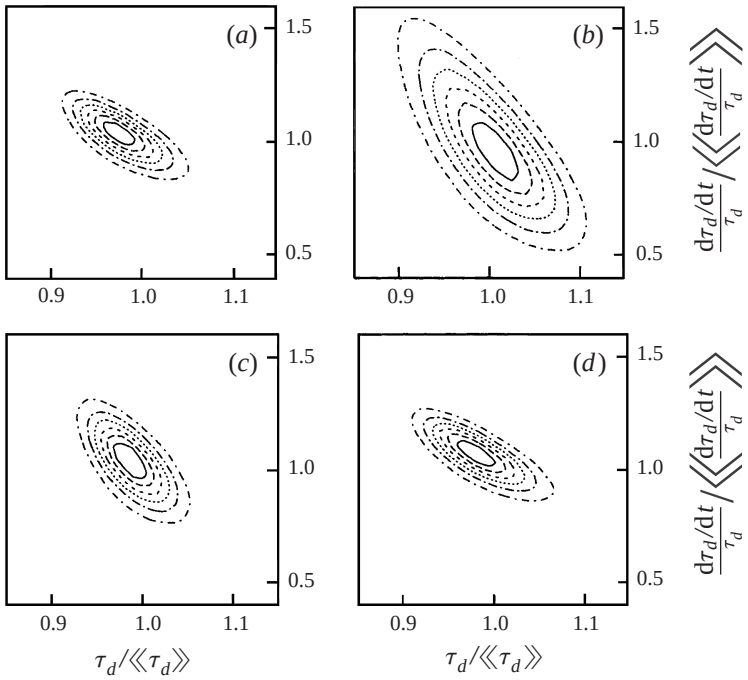

FIGURE 17. Contours of the joint p.d.f. of the evaporation rate and the droplet time constant at $St = 14$. (*a*) The base case; contour levels from 9.63 to 57.8 with increment 9.63. (*b*) $\Phi_{m0} = 4\Phi_{m0b}$; contour levels from 2.61 to 15.66 with increment 2.61. (*c*) $Da = 0.2Da_b$; contour levels from 7.1 to 42.6 with increment 7.1. (*d*) $Ce = 1.5Ce_b$; contour levels from 8.67 to 52.0 with increment 8.67. The highest value belongs to the innermost contour.

on the size of the droplets and is enhanced for droplet time constants of the order of the Kolmogorov time scale. According to figure 4(*b*), the mean value of τ_d/τ_k is ~ 0.5 for the case with $\tau_{d0} = 0.5\tau_{d0b}$ at $St = 12$, and ~ 1.15 for the case with the larger initial droplet size at $St = 14$. Figure 16(*a*) clearly shows that this difference in the droplet size has resulted in a decrease in the preferential distribution for the case with $\tau_{d0} = 0.5\tau_{d0b}$. Changes in other parameters do not seem to have a significant effect on the preferential distribution of the droplets. This suggests that the primary parameter influencing the distribution of the droplets is the ratio of the droplet time constant and the Kolmogorov time scale. Figure 16(*b*) shows that the reaction rate is (moderately) higher in high-strain-rate regions. This should be mainly due to the larger concentration of the droplets there – note that the correlation between the reaction rate and high-strain-rate regions is smaller for the case with $\tau_{d0} = 0.5\tau_{d0b}$. Another possible reason for this phenomenon is that based on the continuum theory coexistence of the reactants is a necessary condition for chemical reaction. This is achieved by molecular diffusion which can be enhanced by bringing the isoscalar lines closer in high-strain-rate regions. This has been observed in previous studies of single-phase reacting flows (see e.g. Leonard & Hill 1992). Figure 16(*b*) also shows a decrease in the correlation between the reaction rate and high-strain-rate regions for the case with smaller Damköhler number. This could be attributed to the broadening of the reaction zone at small Da that will be discussed later in this section.

Due to the variations in the size of the droplets, simulations with reacting droplets provide a convenient means to investigate the effects of the droplet size on the

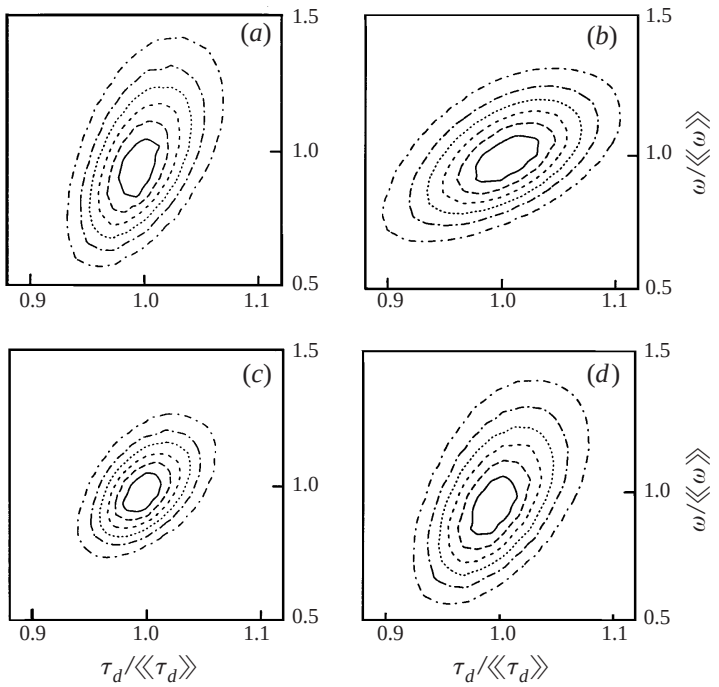

FIGURE 18. Contours of the joint p.d.f. of the reaction rate and the droplet time constant at $St = 14$. (*a*) The base case; contour levels from 3.61 to 21.7 with increment 3.61. (*b*) $\Phi_{m0} = 4\Phi_{m0b}$; contour levels from 3.2 to 19.2 with increment 3.2. (*c*) $Da = 0.2Da_b$; contour levels from 6.38 to 38.3 with increment 6.38. (*d*) $Ce = 1.5Ce_b$; contour levels from 3.26 to 19.6 with increment 3.26. The highest value belongs to the innermost contour.

rates of evaporation and reaction. Figure 17 shows the contours of the Lagrangian joint p.d.f. of the normalized droplet time constant $\tau_d/\langle\langle\tau_d\rangle\rangle$ and the normalized evaporation rate $[(\mathrm{d}\tau_d/\mathrm{d}t)/\tau_d]/\langle\langle[(\mathrm{d}\tau_d/\mathrm{d}t)/\tau_d]\rangle\rangle$. A variety of cases are considered at $St = 14$. It is observed that in all of the cases there is a higher probability to attain larger evaporation rate (per mass of the droplet) for smaller droplets. This is because smaller droplets have a larger surface area to volume ratio. Since the evaporated mass is proportional to the surface area, smaller droplets evaporate more mass per volume and $(\mathrm{d}\tau_d/\mathrm{d}t)/\tau_d$ increases with the decrease of the size of the droplet. Nevertheless, it is noted from figure 17 that a range of evaporation rates is associated with each droplet size. This range widens with the increase of the mass loading ratio or the decrease of the Damköhler number. The change in the heat release coefficient does not show a significant effect.

To investigate the correlation between the droplet size and the reaction rate, in figure 18 the contours of the Lagrangian joint p.d.f. of $\tau_d/\langle\langle\tau_d\rangle\rangle$ and $\omega/\langle\langle\omega\rangle\rangle$ are presented for the same cases and time as those in figure 17. According to figure 18, there is a clear tendency for high reaction rates to occur in the regions of the flow containing larger droplets. In order to find the reason for this phenomenon, in figure 19 the contours of the joint p.d.f.s of the droplet time constant with the fuel vapour mass fraction and the oxidizer mass fraction are shown for the case with the highest mass loading ratio; similar trends were observed for other cases. These variables are considered as they directly appear in the relation for the reaction rate: $\omega = \rho^2 Da Y_{fv} Y_{ox}$. A glance at figure 19 makes it clear that only the fuel vapour

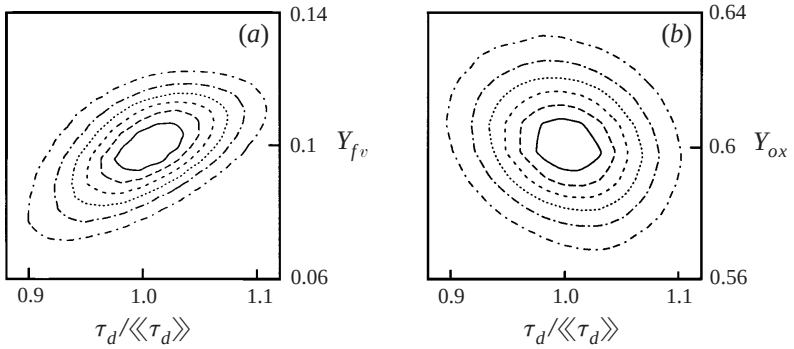

FIGURE 19. Contours of the joint p.d.f. of the droplet time constant and (*a*) the fuel vapour mass fraction; contour levels from 41 to 246 with increment 41, and (*b*) the oxidizer mass fraction; contour levels from 28.7 to 172 with increment 28.7, for the case with $\Phi_{m0} = 4\Phi_{m0b}$ at $St = 14$. The highest value belongs to the innermost contour.

mass fraction exhibits a behaviour similar to that of the reaction rate. Although figure 17 shows that the rate of evaporation per unit mass of the droplet is larger for smaller droplets, the total evaporated mass is larger for larger droplets. This increases the fuel vapour mass fraction in the vicinity of larger droplets and results in the increase of the reaction rate. It is also noted in figure 19(*b*) that the oxidizer mass fraction has smaller values in the neighbourhood of larger droplets. This is due to larger reaction rates which enhance the consumption of the oxidizer in the regions near larger droplets. Since, unlike the fuel vapour, there is no source for generating oxidizer, the mass fraction of the oxidizer decreases as the reaction proceeds.

Next, we study the reaction zone by considering the contours (colour shading) of the reaction rate shown in figure 20 for various cases. These contours are shown in two planes of the flow, (x, y) and (y, z) ($x \equiv x_1, y \equiv x_2, z \equiv x_3$), while the third coordinate is equal to π (half of the simulation domain size). The colour shading changes from red to dark blue as the reaction rate varies from the highest to the lowest values. Superimposed on the contours of the reaction rate are the droplets at their instantaneous locations. The droplets used in these figures are those contained in a slice of the flow that has the thickness of one cell centred at the same plane as that considered for the reaction rate. It must be mentioned that the droplets are not shown in their actual sizes and collision among the droplets is very rare in these simulations. The results in figure 20 are in agreement with those of figure 15 in that the reaction rate is higher in the regions of the flow containing more droplets. Further inspection of figure 20 reveals that the reaction zone is more organized in the direction of the mean flow which only has the component U_1. This is observed in the (x, y)-plane (figure 20*b–f*) for all of the cases. In contrast, figure 20(*a*) shows that the reaction zone in the (y, z)-plane is organized according to the preferential distribution of the droplets in high-strain-rate regions of the flow. The preferred organization of the reaction zone in the presence of a homogeneous shear has been previously studied in single-phase flows (Nomura & Elgobashi 1992; Leonard & Hill 1992). These previous studies show that the intense reaction zone is associated with various vortex structures, and that scalar gradients tend to align with the direction of the most compressive principal strain rate. However, as demonstrated by figure 20, in two-phase flows the influence of the mean flow on the structure of the reaction zone is more pronounced due to the alignment of the droplets with the mean flow direction. A comparison of

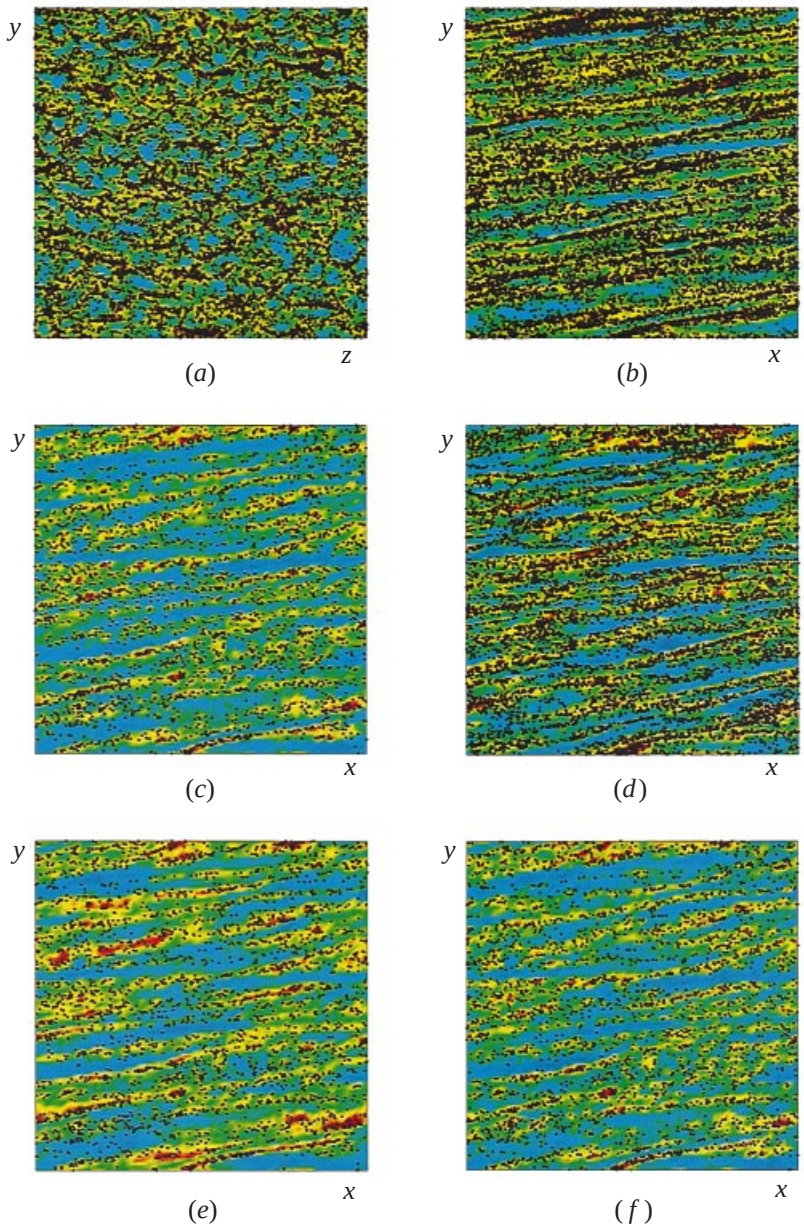

FIGURE 20. Contour plots (colour shadings) of the reaction rate and the instantaneous droplet locations for the case with $\Phi_{m0} = 4\Phi_{m0b}$ in (a, b), for the base case in (c), for $\tau_{d0} = 0.5\tau_{d0b}$ in (d), for $Da = 0.2Da_b$ in (e), and for the case with $Ce = 1.5Ce_b$ in (f). The highest and the lowest reaction rates are shown by red and dark blue, respectively. The droplets are not shown at their actual sizes. Part (d) at $St = 12$, all other parts at $St = 14$.

figure 20(e) and (c) shows that the reaction zone is broader for the case with smaller Damköhler number. This is in agreement with previous observations in single-phase reacting flows (Swaminathan *et al.* 1996). A close inspection of figure 20 indicates that some of the droplets are located in regions of low reaction rate. Further analysis of the dispersed phase via consideration of the size of the droplets, revealed that these

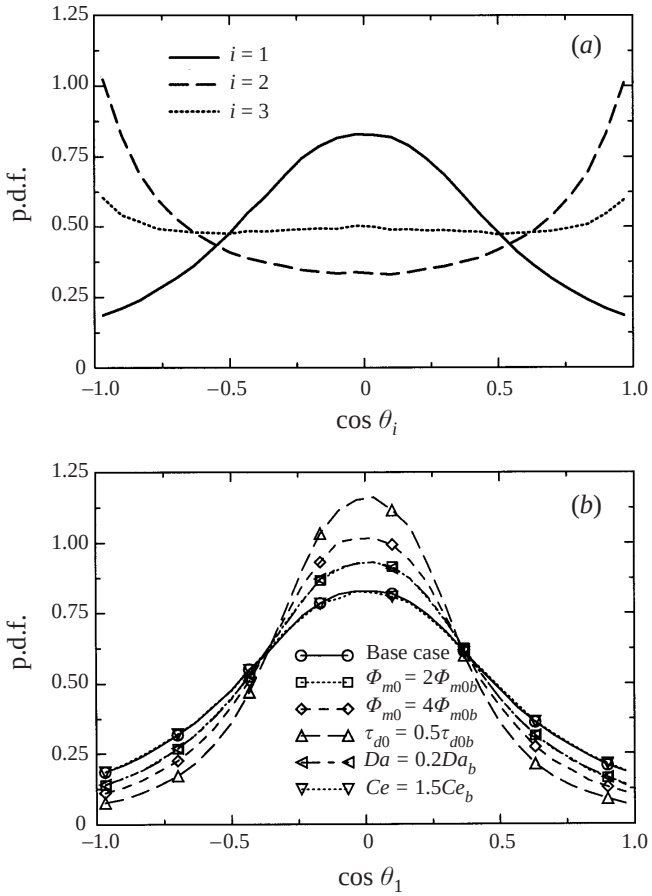

FIGURE 21. The p.d.f.s of the cosine of the angle between the coordinate axes and the gradient of the reaction rate at $St = 14$. (*a*) The base case in various directions. (*b*) Various cases in the x_1-direction.

droplets have small sizes and do not significantly contribute to the production of the fuel vapour. This analysis also showed that the regions of intense reaction rate are associated with larger droplets.

To further investigate the effects of the large scales of the flow on the reaction zone, the alignment of the gradient of the reaction rate, $\nabla\omega$, with coordinate axes, x_i, is considered. Figure 21(*a*) shows the p.d.f. of $\cos\theta_i$, where θ_i is defined as the angle between $\nabla\omega$ and x_i, for the base case at $St = 14$. The figure clearly shows that the gradient of the reaction rate tends to align perpendicularly to the direction of the mean flow as the highest probability is around $\cos\theta_1 = 0$ and $\cos\theta_2 = \pm 1$. This is in agreement with the results in figure 20 showing that the contours of the reaction rate are mostly aligned with the mean flow direction, x_1. The p.d.f. for $i = 3$ also verifies the results in figure 20 that in the (y, z)-plane there is no preferred direction for the reaction zone. The effects of various parameters on the organization of the reaction zone with the mean flow direction are portrayed in figure 21(*b*) which shows the p.d.f. of $\cos\theta_1$ at $St = 14$. It is observed that the alignment is enhanced with the increase of the mass loading ratio or the decrease of the droplet time constant. The decrease of the Damköhler number also results in the increase of the alignment of the reaction

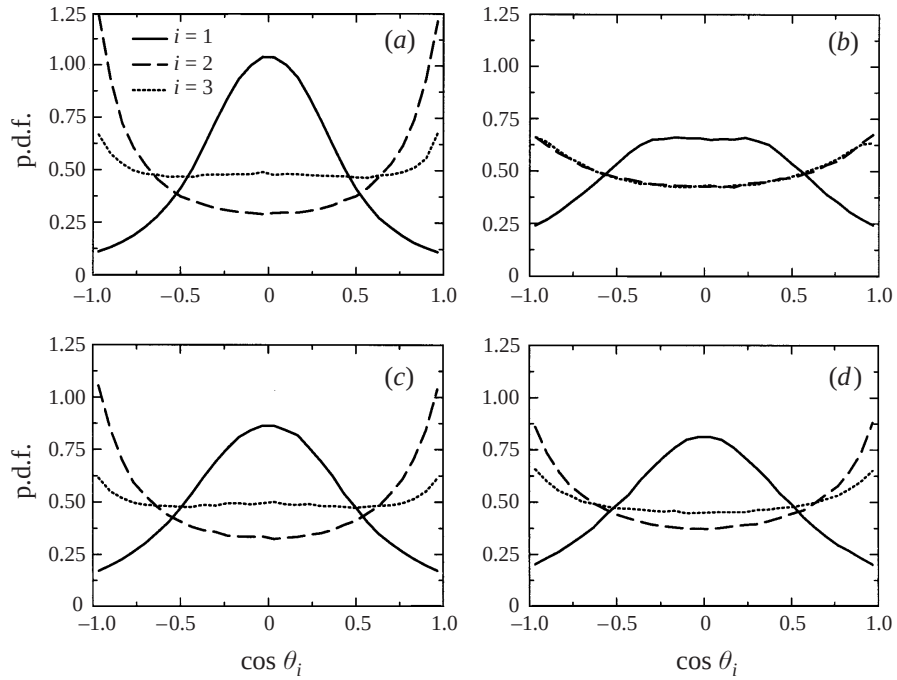

FIGURE 22. The p.d.f.s of the cosine of the angle between the coordinate axes and the gradient of the fuel vapour mass fraction, in (a, c), and the oxidizer mass fraction, in (b, d), at $St = 14$: (a, b) the evaporating case, (c, d) the base case.

zone with the mean flow direction. This may seem inconsistent with the fact that the time scale of the reaction increases with the decrease of Da and could provide the droplets with more time to leave the reaction zone, thus decreasing the correlation between the reaction zone and the droplet distribution. However, the decrease of the evaporation rate, associated with the decrease of the Damköhler number, provides more oxidizer in the vicinity of the droplets and facilitates the chemical reaction (see the discussion accompanying figure 15). In fact, all of the cases that exhibit a stronger alignment evaporate less mass per droplet compared to the base case.

Figure 22 provides some insight into the effects of the mean shear on the mass fractions of the fuel vapour and the oxidizer by showing the p.d.f.s of the cosine of the angle between the gradient of these variables and the coordinate axes. Here, both the base case and its corresponding evaporating (non-reacting) case at $St = 14$ are considered in order to also assess the role of the chemical reaction. Figure 22(a) for the non-reacting case shows that the fuel vapour is largely aligned with the direction of the mean flow. This could be due to the effects of the mean flow both on the fuel vapour as a scalar field as well as on the droplets as a dispersed phase. Since no simulation of single-phase flow has been performed in this study, it is not possible to clearly distinguish between these two mechanisms. However, it can be stated that, due to the presence of the droplets, the tendency of the fuel vapour to align with the direction of the mean flow should be larger in two-phase flow than in single-phase flow. Some support for this statement can be provided by comparing the p.d.f.s for the oxidizer in the same case with those of the fuel vapour. Figure 22(b) clearly shows that the alignment of the oxidizer with the mean flow is smaller than that of the fuel vapour. Since the oxidizer is not as strongly affected by the droplets as the fuel

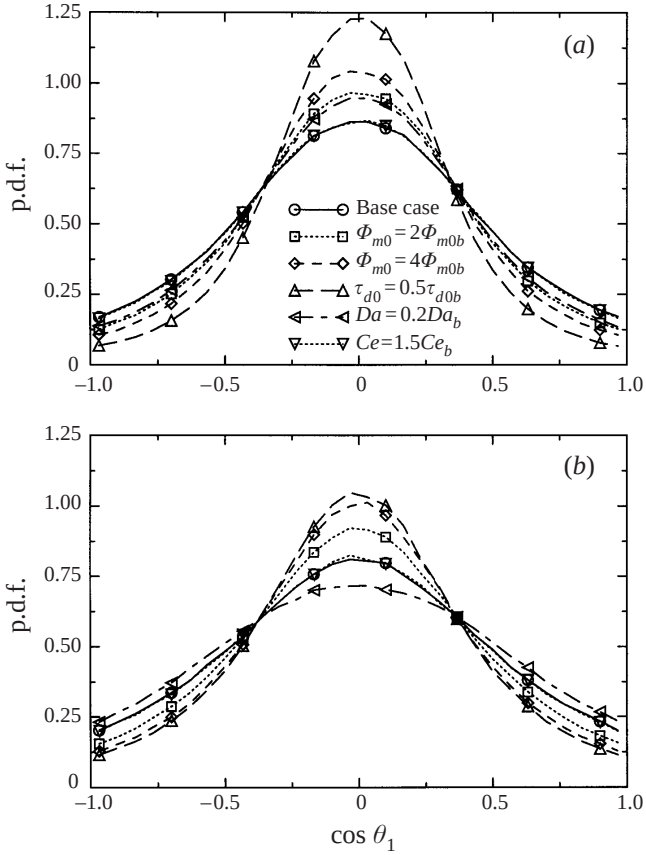

FIGURE 23. The p.d.f.s of the cosine of the angle between the x_1-direction and the gradient of the reactants at $St = 14$. (*a*) The fuel vapour mass fraction and (*b*) the oxidizer mass fraction.

vapour, the difference observed between figures 22(*a*) and 22(*b*) may be attributed to the effects of the droplets. The scenario is significantly changed in the presence of the chemical reaction. Figures 22(*c*) and 22(*d*) show that the p.d.f.s for the fuel vapour and the oxidizer in the reacting case are much closer compared to those in the non-reacting case. Therefore, chemical reaction decreases the alignment of the fuel vapour with the mean flow direction while increasing that of the oxidizer. This is in agreement with the discussion in § 4 that chemical reaction tends to bring the fuel vapour and the oxidizer closer. It is also noted in figure 22 that the effects of chemical reaction on the p.d.f.s in the $i = 3$ direction is not significant.

To investigate the effects of various parameters on the alignment of the reactants with the mean flow direction, in figure 23 we consider the p.d.f. of $\cos\theta_1$ at $St = 14$. It is observed that the height of the p.d.f. for both reactants increases with the increase of the mass loading ratio or the decrease of the droplet time constant. The decrease of the Damköhler number increases the alignment of the fuel vapour while decreasing the alignment of the oxidizer. This is expected as the alignment of the oxidizer is through reaction which becomes weaker with the decrease of *Da*. The change in the heat release coefficient does not show any significant impact on the alignment. With the exclusion of the case with smaller *Da*, the trends in figure 23 are in agreement with those in figure 15. A comparison of the two figures shows that an increase in the correlation between the reaction rate and the droplet density corresponds to an

increase in the alignment of the reactants with the mean flow direction. As was argued earlier, this behaviour can be explained by considering the changes in the evaporation rate in various cases.

6. Summary and concluding remarks

Evaporation and combustion of fuel droplets dispersed in a compressible oxidizer gas are investigated while considering a two-way coupling between the phases. Direct numerical simulation is used to solve for the mixture of the oxidizer gas, the fuel vapor, and the product in the Eulerian frame; the dispersed phase is treated in the Lagrangian frame. The problem is considered in the context of homogeneous shear flow at low Mach numbers without the presence of shocklets. It is assumed that combustion takes place in the vapour phase and can be described by a single-step, second-order, irreversible reaction. Several cases are simulated to investigate the effects of the mass loading ratio, the droplet time constant, the Damköhler number, and the heat release coefficient on the droplet size, the reactants, and the reaction rate and zone.

The analysis of the flow statistics, including various power spectra, indicates that the Eulerian fields are well-resolved and that the assumptions adopted in the formulation of the dispersed phase are satisfied throughout the simulations. The rate of evaporation varies for different cases; however, the size of the droplets may be reasonably described by a normal distribution, after the effects of the initial conditions have subsided. The increase of the mass loading ratio increases the r.m.s. of the droplet diameter while decreasing its skewness to negative values. The joint p.d.f. of the fuel vapour mass fraction and the droplet number density shows the presence of the fuel vapour in the regions of the flow that do not contain any droplets. The analysis of the joint p.d.f. of the fuel vapour and the oxidizer mass fractions indicates that the reaction can be categorized as premixed. Despite the chemical reaction between the fuel vapour and the oxidizer, the mean mass fraction of the fuel vapour increases in time for the parameter values used in the simulations. By decreasing the reaction rate, the decrease of the Damköhler number results in the increase of the fuel vapour mass fraction despite a smaller rate of evaporation. The r.m.s. of the fuel vapour mass fraction exhibits an increasing trend for most of the time whereas that of the oxidizer decreases continuously. The difference between the Taylor length scale of the fuel vapour and that of the oxidizer decreases in time in the presence of the chemical reaction. This is not the case when the droplets are only evaporating without combustion.

The reaction rate is higher in the regions of the flow with larger droplet concentration. There is also a tendency for higher reaction rates to occur in the regions of the flow with high strain rate. The evaporation rate (per mass of the droplet) is higher for smaller droplets whereas the opposite is true for the reaction rate. The latter is a result of the higher values of the fuel vapour mass fraction in the regions of the flow containing larger droplets. The contour plots of the reaction rate in various planes of the flow indicate that the reaction zone is aligned with the direction of the mean flow. This is due mainly to the effects of the mean shear on the dispersed droplets, and is also verified by the analysis of the p.d.f.s of the angle between the gradient of the reaction rate and the coordinate axes. The alignment is enhanced with the increase of the mass loading ratio or the decrease of the droplet time constant. The decrease of the Damköhler number also results in the increase of the alignment of the reaction zone with the mean flow direction. Similar p.d.f.s for the fuel vapour and oxidizer mass fractions show that, without the chemical reaction, the fuel vapour is more aligned with the mean flow direction than is the oxidizer. The chemical reaction decreases (increases) the alignment of the fuel vapour (oxidizer) with the direction of the mean flow.

From a modelling standpoint, the results presented here can be very useful for model development and may also be considered for model assessment. However, it must be emphasized that some of the trends observed in the results strongly depend on the specific values used for various parameters, and should by no means be considered 'universal'. This is in particular true for the values of the Damköhler number and the heat release coefficient which greatly affect the rate of reaction and the variations of the temperature. The behaviour of the two-phase turbulent reacting flow depends on the time scales of turbulence, evaporation, reaction, and droplet dispersion. The current limitation in computational resources does not allow a complete investigation of the problem while considering a wide range of variations for various parameter values. Therefore, future use of DNS for two-phase turbulent reacting flows is recommended.

The support for this work was provided by the US Office of Naval Research under Grant N00014-99-1-0808 with Dr G. D. Roy as Technical Monitor, and by the National Science Foundation under Grant CTS-9874655 with Dr M. C. Roco as Program Director. Computational resources were provided by the San Diego Supercomputing Center.

REFERENCES

Balakrishnan, G., Sarkar, S. & Williams, F. A. 1995 Direct numerical simulation of diffusion flames with large heat release in compressible homogeneous turbulence. *AIAA Paper* 95-2375.

Bilger, R. W. 1980 Turbulent flows with nonpremixed reactants. In *Turbulent Reacting Flows* (ed. P. A. Libby & F. A. Williams). Topics in Applied Physics, vol. 44, chap. 3, pp. 65–113. Springer.

Bird, R. B., Stewart, W. E. & Lightfoot, E. N. 1960 *Transport Phenomena.* Wiley.

Blaisdell, G. A., Mansour, N. N. & Reynolds, W. C. 1991 Numerical simulation of compressible homogeneous turbulence. *Dept of Mechanical Engineering Rep.* TF-50. Stanford University, Stanford, CA.

Blaisdell, G. A., Mansour, N. N. & Reynolds, W. C. 1993 Compressibility effects on the growth and structure of homogeneous turbulent shear flow. *J. Fluid Mech.* **256**, 443–485.

Brooke, J. W., Kontomaris, K., Hanratty, T. J. & McLaughlin, J. B. 1992 Turbulent deposition and trapping of aerosols at a wall. *Phys. Fluids* **4**, 825–834.

Brooke, J. W., Hanratty, T. J. & McLaughlin, J. B. 1994 Free-flight mixing and deposition of aerosols. *Phys. Fluids* **6**, 3404–3415.

Chen, M. & McLaughlin, J. B. 1995 A new correlation for the aerosol deposition rate in vertical ducts. *J. Colloid Interface Sci.* **169**, 437–455.

Chen, M., Kontomaris, K. & McLaughlin, J. B. 1995 Dispersion, growth, and deposition of coalescing aerosols in a direct numerical simulation of turbulent channel flow. ASME FED vol. 228, pp. 27–32.

Chiu, H. H. & Liu, T. M. 1977 Group combustion of liquid droplets. *Combust. Sci. Tech.* **17**, 127–142.

Crowe, C. T., Sharma, M. P. & Stock, D. E. 1977 The Particle-Source in Cell (PSI-Cell) model for Gas-Droplet flows. *Trans. ASME* I: *J. Fluids Engng* **6**, 325–332.

Crowe, C. T., Troutt, T. R. & Chung, J. N. 1996 Numerical models for two-phase turbulent flows. *Ann. Rev. Fluid Mech.* **28**, 11–43.

Eaton, J. K. & Fessler, J. R. 1994 Preferential concentration of particles by turbulence. *Intl J. Multiphase Flow Suppl.* **20**, 169–209.

Elghobashi, S. & Truesdell, G. C. 1992 Direct simulation of particle dispersion in a decaying isotropic turbulence. *J. Fluid Mech.* **242**, 655–700.

Elghobashi, S. & Truesdell, G. C. 1993 On the two-way interaction between homogeneous turbulence and dispersed solid particles. I: Turbulence modification. *Phys. Fluids* **5**, 1790–1801.

Gao, F. & O'Brien, E. E. 1991 Direct numerical simulations of reacting flows in homogeneous turbulence. *AIChE J.* **37**, 1459–1470.

GIVI, P. & MCMURTRY, P. A. 1988 Non-premixed reaction in homogeneous turbulence: Direct numerical simulations. *AIChE J.* **34**, 1039–1042.

GIVI, P. 1989 Model free simulations of turbulent reactive flows. *Prog. Energy Combust. Sci.* **15**, 1–107.

GIVI, P. 1994 Spectral and random vortex methods in turbulent reacting flows. In *Turbulent Reacting Flows* (ed. P. A. Libby & F. A. Williams), chap. 8, pp. 475–572. Academic.

HILL, J. C. 1979 Simulation of chemical reaction in a turbulent flow. In *Proc. Second R. F. Ruth Chemical Engineering Research Symp., Ames, Iowa*, pp. 27–53.

JABERI, F. A., MILLER, R. S., MASHAYEK, F. & GIVI, P. 1997 Differential diffusion in binary scalar mixing and reaction. *Combust. Flame* **109**, 561–577.

JABERI, F. A. 1996 Mathematical modelling and computational analysis of turbulent mixing and reacting systems. PhD Thesis, Department of Mechanical and Aerospace Engineering, State University of New York at Buffalo.

KIDA, S. & ORSZAG, S. A. 1990 Energy and spectral dynamics in forced compressible turbulence. *J. Sci. Comput.* **5**, 85–125.

KIDA, S. & ORSZAG, S. A. 1992 Energy and spectral dynamics in decaying compressible turbulence. *J. Sci. Comput.* **7**, 1–34.

LEE, S., LELE, S. K. & MOIN, P. 1991 Eddy shocklets in decaying compressible turbulence. *Phys. Fluids* A **3**, 657–664.

LEONARD, A. D. & HILL, J. C. 1991 Scalar dissipation and mixing in turbulent reacting flows. *Phys. Fluids* A **3**, 1286–1299.

LEONARD, A. D. & HILL, J. C. 1992 Mixing and chemical reaction in sheared and nonsheared homogeneous turbulence. *Fluid Dyn. Res.* **10**, 273–297.

LING, W., CHUNG, J. N., TROUTT, T. R. & CROWE, C. T. 1997 *Numerical Simulation of Particle Dispersion in a Three-Dimensional Temporal Mixing Layer*. ASME FED SM 97-3182.

LUMLEY, J. L. 1978 Two-phase and non-newtonian flows. *Topics Phys.* **12**, 290–324.

MASHAYEK, F. & JABERI, F. A. 1999 Particle dispersion in forced isotropic low-Mach-number turbulence. *Intl J. Heat Mass Transfer*, **42**, 2823–2836.

MASHAYEK, F., JABERI, F. A., MILLER, R. S. & GIVI, P. 1997 Dispersion and polydispersity of droplets in stationary isotropic turbulence. *Intl J. Multiphase Flow* **23**, 337–355.

MASHAYEK, F., TAULBEE, D. B. & GIVI, P. 1998 Modelling and simulation of two-phase turbulent flow. In *Propulsion Combustion: Fuels to Emissions* (ed. G. D. Roy), chap. 8, pp. 241–280. Taylor & Francis.

MASHAYEK, F., BARRÉ, C. & TAULBEE, D. B. 1999 Direct numerical simulation of particle-laden homogeneous plain strain turbulent flow. In *Proc First Intl Symp. on Turbulence and Shear Flow Phenomena, Santa Barbara, CA* (ed. S. Banerjee & J. K. Eaton), pp. 115–120. Begell House.

MASHAYEK, F. 1998*a* Droplet-turbulence interactions in low-Mach-number homogeneous shear two-phase flows. *J. Fluid Mech.* **376**, 163–203.

MASHAYEK, F. 1998*b* Direct numerical simulations of evaporating droplet dispersion in forced low Mach number turbulence. *Intl J. Heat Mass Transfer* **41**, 2601–2617.

MAXEY, M. R. & PATEL, B. K. 1997 Forced-coupled simulations of particle suspensions at zero and finite Reynolds numbers. *Center for Fluid Mechanics* Rep. 97-2, Brown University, Providence, RI.

MAXEY, M. R., PATEL, B. K., CHANG, E. J. & WANG, L. P. 1997 Simulations of dispersed turbulent multiphase flow. *Fluid Dyn. Res.* **20**, 143–156.

MCLAUGHLIN, J. B. 1989 Aerosol particle deposition in numerically simulated channel flow. *Phys. Fluids* A **1**, 1211–1224.

MCLAUGHLIN, J. B. 1994 Numerical computation of particles-turbulence interaction. *Intl J. Multiphase Flow Suppl.* **20**, 211–232.

MCMURTRY, P. A. & GIVI, P. 1989 Direct numerical simulations of mixing and reaction in a nonpremixed homogeneous turbulent flow. *Combust. Flame* **77**, 171–185.

MCMURTRY, P. A., JOU, W.-H., RILEY, J. J. & METCALFE, R. W. 1986 Direct numerical simulations of a reacting mixing layer with chemical heat release. *AIAA J.* **24**, 962–970.

MENON, S. & FERNANDO, E. 1990 A numerical study of mixing and chemical heat release in supersonic mixing layers. *AIAA Paper* 90-0152.

MILLER, R. S. & BELLAN, J. 1999 Direct numerical simulation of a confined three-dimensional

gas mixing layer with one evaporating hydrocarbon-droplet laden stream. *J. Fluid Mech.* **384**, 293–338.

Miura, H. & Kida, S. 1995 Acoustic energy exchange in compressible turbulence. *Phys. Fluids* **7**, 1732–1742.

Nomura, K. K. & Elgobashi, S. E. 1992 Mixing characteristics of an inhomogeneous scalar in isotropic and homogeneous sheared turbulence. *Phys. Fluids* A **4**, 606–625.

Ounis, H., Ahmadi, G. & McLaughlin, J. B. 1991 Dispersion and deposition of Brownian particles from point sources in a simulated turbulent channel flow. *J. Colloid Interface Sci.* **147**, 233–250.

Ounis, H., Ahmadi, G. & McLaughlin, J. B. 1993 Brownian particle deposition in a directly simulated turbulent channel flow. *Phys. Fluids* **5**, 1427–1432.

Pan, Y. & Banerjee, S. 1996 Numerical simulation of particle interactions with wall turbulence. *Phys. Fluids* **8**, 2733–2755.

Passot, T. & Pouquet, A. 1987 Numerical simulation of compressible homogeneous flows in the turbulent regime. *J. Fluid Mech.* **181**, 441–466.

Pedinotti, S., Mariotti, G. & Banerjee, S. 1992 Direct numerical simulation of particle behaviour in the wall region of turbulent flows in horizontal channels. *Intl J. Multiphase Flow* **18**, 927–941.

Riley, J. J. & Patterson, G. S. 1974 Diffusion experiments with numerically integrated isotropic turbulence. *Phys. Fluids* **17**, 292–297.

Rogallo, R. S. 1981 Numerical experiments in homogeneous turbulence. *NASA TM* 81315.

Rouson, D. W. I. & Eaton, J. K. 1994 Direct numerical simulation of particles interacting with a turbulent channel flow. In *Proc. 7th Workshop on Two-Phase Flow Predictions, Erlangen, Germany* (ed. M. Sommerfeld).

Rouson, D. W. I., Eaton, J. K. & Abrahamson, S. D. 1997 A direct numerical simulation of a particle-laden turbulent channel flow. *Dept of Mechanical Engineering Rep.* TSD-101, Stanford University, Stanford, CA.

Samimy, M. & Lele, S. K. 1991 Motion of particles with inertia in a compressible free shear layer. *Phys. Fluids* **3**, 1915–1923.

Sarkar, S., Erlebacher, G. & Hussaini, M. Y. 1991 Direct simulation of compressible turbulence in a shear flow. *ICASE Rep.* 91-29. NASA Langley Research Center, Hampton, VA.

Sarkar, S., Erlebacher, G. & Hussaini, M. Y. 1992 Compressible homogeneous shear: Simulation and modeling. *ICASE Rep.* 92-6. NASA Langley Research Center, Hampton, VA.

Sarkar, S. 1994 The stabilizing effect of compressibility in turbulent shear flow. *ICASE Rep.* 94-46. NASA Langley Research Center, Hampton, VA.

Simonin, O., Deutsch, E. & Boivin, M. 1995 Large eddy simulation and second-moment closure model of particle fluctuating motion in two-phase turbulent shear flows. In *Turbulent Shear Flows 9* (ed. F. Durst, N. Kasagi, B. E. Launder, F. W. Schmidt & J. E. Whitelaw), pp. 85–115. Springer.

Squires, K. D. & Eaton, J. K. 1990 Particle response and turbulence modification in isotropic turbulence. *Phys. Fluids* A **2**, 1191–1203.

Squires, K. D. & Eaton, J. K. 1991*a* Measurements of particle dispersion obtained from direct numerical simulations of isotropic turbulence. *J. Fluid Mech.* **226**, 1–35.

Squires, K. D. & Eaton, J. K. 1991*b* Preferential concentration of particles by turbulence. *Phys. Fluids* A **3**, 1169–1178.

Swaminathan, N., Mahalingam, S. & Kerr, R. M. 1993 Direct numerical simulation of reversible and irreversible chemical reaction in turbulent nonpremixed flames. *AIAA Paper* 93-0103.

Swaminathan, N., Mahalingam, S. & Kerr, R. M. 1996 Structure of nonpremixed reaction zones in numerical isotropic turbulence. *Theor. Comput. Fluid Dyn.* **8**, 201–218.

Taulbee, D. B., Mashayek, F., Givi, P. & Barré, C. 1997 Simulation and Reynolds stress modeling of particle-laden turbulent shear flows. In *Proc. 11th Symp. on Turbulent Shear Flows, Grenoble, France*.

Truesdell, G. C. & Elghobashi, S. 1994 On the two-way interaction between homogeneous turbulence and dispersed solid particles. II: Particle dispersion. *Phys. Fluids* **6**, 1790–1801.

Turns, S. R. 1996 *An Introduction to Combustion: Concepts and Applications.* McGraw-Hill.

Wallis, G. B. 1969 *One Dimensional Two Phase Flow*. McGraw Hill.

Wang, L.-P. & Maxey, M. R. 1993 Settling velocity and concentration distribution of heavy particles in isotropic turbulence. *J. Fluid Mech.* **256**, 27–68.